arXiv:astro-ph/0701279v1 10 Jan 2007

A KECK SURVEY FOR GRAVITATIONALLY-LENSED LYMAN α EMITTERS IN THE REDSHIFT RANGE 8.5<Z<10.4: NEW CONSTRAINTS ON THE CONTRIBUTION OF LOW LUMINOSITY SOURCES TO COSMIC REIONIZATION

Daniel P. Stark[1], Richard S. Ellis[1], Johan Richard [1], Jean-Paul Kneib [1,2], Graham P. Smith [1,3], Michael R. Santos [4]

Draft version January 10, 2007

ABSTRACT

We discuss new observational constraints on the abundance of faint high redshift Lyman-α emitters secured from a deep Keck near-infrared spectroscopic survey which utilizes the strong magnification provided by lensing galaxy clusters at intermediate redshift ($z = 0.2 - 0.5$). In each of 9 clusters we have undertaken a systematic 'blind' search for line emission with NIRSPEC in the J-band within carefully-selected regions which offer very high magnifications ($\gtrsim \times$10-50) for background sources with redshifts $z \simeq 10$. The high magnification enables the detection of emission at unprecedented flux limits (10^{41} - 10^{42} erg s^{-1}), much fainter than those of conventional narrow band imaging and other spectroscopic searches. As the comoving volumes probed are small, our survey is designed to address the important question of whether intrinsically feeble star forming galaxies could provide the dominant ionizing flux at $z \sim 10$. Our survey has yielded six promising ($> 5\sigma$) candidate Lyman-α emitters which lie between $z = 8.7$ and $z = 10.2$. We carefully discuss the validity of our detections in the light of earlier, apparently false, claims. We then focus on the likelihood that the detected line is Lyman-α from a distant lensed-source. All but one of the candidates remain undetected in deep HST optical images and lower redshift line interpretations can be excluded, with reasonable assumptions, through the non-detection of secondary emission in further spectroscopy undertaken with LRIS and NIRSPEC. We demonstrate that rigorous confirmation of the Lyman-α hypothesis for all of our candidates will be a challenge with current facilities. Nonetheless, as a result of our tests, we argue that at least two of our candidates are likely to be at $z \simeq 10$. Given the small survey volume, this suggests there is a large abundance of low luminosity star-forming sources occupying the era when the reionization process is thought, from independent evidence, to be ongoing. While the predicted reionization photon budget depends upon a large number of physical assumptions, our first glimpse at the $z \simeq 10$ Universe suggests that low luminosity star-forming galaxies contribute a significant proportion of the UV photons necessary for cosmic reionization.

Subject headings: cosmology: observations — galaxies: evolution — galaxies: formation — galaxies: high-redshift — gravitational lensing

1. INTRODUCTION

After the epoch of recombination at z≃1000, neutral hydrogen permeated the universe. The earliest observable structure dates back to the beginning of this era at the surface of last scattering traced by the cosmic microwave background (CMB). The next most distant observable represent the populations of galaxies, gamma-ray bursts, and quasars at $z \simeq 6.2 - 7.0$ (Hu et al. 2002; Iye et al. 2006; Totani et al. 2006; Kashikawa et al. 2006; Fan et al. 2006; Bouwens & Illingworth 2006). The interval between $z \simeq 1000$ and $z \simeq 6.5$ contains many landmark events: the formation of the first stars, the assembly of first galaxies, the growth of the first supermassive black holes that power quasars, and the reionization of neutral hydrogen in the intergalactic medium. One of the primary driving forces in observational cosmology today is to illuminate the growth of these first structures in this important, but poorly understood, era.

Recently, important constraints have emerged on the extent of star formation activity that occurred in the latter part of this era. The WMAP temperature-polarization cross correlation signal on large angular scales (Spergel et al. 2006) implies scattering of microwave photons by free electrons from ionizing sources at $z \simeq 10 - 12$, suggesting an early period of efficient star formation. Meanwhile, Hubble Space Telescope (HST) and Spitzer observations have uncovered a population of very massive ($M_{stellar} \sim 10^{10}$ - 10^{11} $M_{\odot}$) galaxies at z≃6 with well-established (>100 Myr) stellar populations (Egami et al. 2005; Eyles et al. 2005; Mobasher et al. 2005; Yan et al. 2005; Stark et al. 2006; Eyles et al. 2006; Yan et al. 2006). The assembly of such massive galaxies by these redshifts requires significant star formation at yet earlier times. Observations of z-dropouts and J-dropouts with HST indicate a decline in the star formation activity of luminous Lyman-break galaxies out to $z \simeq 7 - 10$ (Bouwens et al. 2005; Bouwens & Illingworth 2006); if there is significant star formation activity in this redshift interval, these observations indicate it likely occurred in lower-luminosity systems.

Despite these indications of early activity, current fa-

[1] Department of Astrophysics, California Institute of Technology, MS 105-24, Pasadena, CA 91125; dps@astro.caltech.edu
[2] Observatoire Astronomique de Marseille-Provence, Traverse du Siphon - BP 8, 13376 Marseille Cedex 12, France
[3] School of Physics and Astronomy, University of Birmingham, Edgbaston, Birmingham, B15 2TT, UK
[4] Space Telescope Science Institute, 3700 San Martin Drive, Baltimore, MD 21218

cilities are poorly-equipped to undertake conventional searches for star-forming sources beyond $z \simeq 7$. Even with HST and 8 meter class telescopes, continuum ('drop-out') and narrow-band imaging Lyman-α searches probe only the most luminous, rare, sources at these redshifts; the contribution to the reionization flux from these sources may well be small. While narrowband surveys have had significant success at detecting Lyman-α emitters at $z \simeq 6$ (Hu et al. 1998, 2002, 2004; Malhotra & Rhoads 2004; Hu et al. 2005; Stern et al. 2005; Kashikawa et al. 2006; Shimasaku et al. 2006) only one Lyman-α emitter has been convincingly detected at $z \simeq 7$ (Iye et al. 2006). At $z \simeq 9$, narrowband surveys for relatively luminous Lyman-α emitters ($\gtrsim 10^{42.5}$ erg s^{-1}) have yet to find any sources (Willis & Courbin 2005; Cuby et al. 2006). While a few candidate Lyman-break galaxies beyond $z \simeq 7$ have been suggested from photometric data (Bouwens et al. 2005; Labbé et al. 2006; Richard et al. 2006; Bouwens & Illingworth 2006; Henry et al. 2007), none has yet been spectroscopically confirmed, due largely to the difficulties inherent to observing in the near-infrared.

Recent observations of the faint end slope of the star-forming luminosity function at $z \simeq 6$ (Yan & Windhorst 2004; Bouwens et al. 2006) support the suggestion that the bulk of the integrated star formation at high redshift may arise from very low luminosity sources, as expected theoretically (Barkana & Loeb 2001; Wyithe & Loeb 2006). However, forming stars in low mass halos is complicated by a number of feedback effects, any of which could significantly decrease the star formation efficiency. Clarifying whether low luminosity systems are abundant at early times requires observations probing well below the sensitivity limits obtainable with current facilities using conventional methods.

The study of lower luminosity sources rendered visible by the strong gravitational lensing induced by foreground clusters is the only current means to advance this quest before the next generation of telescopes is available. Although a typical lensing cluster magnifies sources by ×5-10 over 1 arcmin^2 for sources at $z > 7$, faint signals can be boosted $> \times 15$ on the so-called *critical line* - the location of the lensing caustic in the image plane. Spectroscopy and detailed studies become feasible at otherwise impossible (unlensed) limits. For several objects recently located via this technique (Ellis et al. 2001; Kneib et al. 2004; Santos et al. 2004; Egami et al. 2005), stellar continuum slopes, Lyman-α profiles and star formation rates have been determined for sources whose intrinsic flux is close to the faintest direct imaging limits so far reached, $I_{AB} \simeq 30$ (Beckwith et al. 2006). Until the availability of more powerful ground and space-based facilities, scanning the critical lines of massive clusters provides possibly the only reliable means of estimating the abundance of low luminosity star forming sources in the $7 < z < 12$ interval over which cosmic reionization is thought to take place.

This paper presents the results of a spectroscopic survey for strongly-lensed Lyman-α emitters at $8.5 < z < 10.4$ using the NIRSPEC near-infrared spectrograph on the Keck II telescope. The survey follows logically from a very similar, successful one undertaken at $z \simeq 4 - 6$ using the LRIS optical spectrograph on the Keck I telescope

(Santos et al. 2004) to which the reader is referred.

A plan of the paper follows. We contrast our lensing search technique with other, more conventional probes of early star forming sources in §2. The NIRSPEC observations and reduction methods are presented in §3. Here we describe the candidate selection criteria and derive the survey sensitivity function. A set of 6 promising candidate $z \simeq 10$ Lyman-α emitters are presented in §4. Here we discuss in detail both the reality of the line detections and the likelihood that the line identifications represent high redshift Lyman-α. Noting the likelihood that a significant fraction of our sources may lie at $z \simeq 10$, we infer the abundance of high redshift low luminosity sources and compare these with other constraints in §5. In §6 we discuss whether the abundance so derived might represent a significant fraction of that necessary to complete cosmic reionization. We present our conclusions in §7.

Throughout the paper, we have assumed a flat universe and $(\Omega_m, \Omega_\Lambda) = (0.27, 0.73)$ following the results presented in the initial WMAP data release (Spergel et al. 2003).

2. GRAVITATIONAL LENSING AND SURVEY STRATEGIES - A CRITIQUE

Strong gravitational lensing by intermediate redshift galaxy clusters offers the capability of extending the current generation of high redshift galaxy surveys so that lower luminosity sources can be brought into view. This added boost in sensitivity is particularly effective at the highest source redshifts ($z \gtrsim 7$) where the bulk of star formation activity may be taking place in low mass dark matter halos (Barkana & Loeb 2001).

Lensing increases the apparent area of a background source while conserving the surface brightness; thus the gain in sensitivity is the magnification factor, $\mathcal{M}$. Rich clusters of galaxies at intermediate redshifts (e.g. $z \simeq 0.2 - 0.5$) amplify high redshift sources by factors of typically $\mathcal{M} \simeq 3 - 5$ over areas of a few arcmin^2. However, boosts of $\mathcal{M} \simeq 10 - 50$ are possible near the *critical line* - the theoretical locus of points in the image plane corresponding to the caustic of infinite magnification. Clusters are usually characterized by both an inner and an outer critical line, the location of which varies as a function of source (background) redshift.

The accurate location on the sky of these critical lines can only be determined in the case of clusters for which detailed mass models are available. Such a mass model is primarily constrained by the positions and redshifts of lensed features (Kneib et al. 1996). A mass model can be validated, for example, by securing spectrosopy of lensed features whose redshifts were predicted by the mass model using an 'inversion' technique (Ebbels et al. 1998). Currently, such high quality mass models are only available for $\simeq$20 clusters; however this should increase in the future with additional surveys (Ebeling et al. 2001).

However, the gain in sensitivity afforded by strong lensing comes with a loss in survey area, compared to an equivalent unlensed survey, by a factor of $\mathcal{M}$. This is an important point as the area of high magnification (say $\mathcal{M} > 10$) is already quite small ($\simeq 0.1$ arcmin^2). Provided, as seems reasonable (§1), that the slope of the faint-end slope of the luminosity function is very steep, then strong lensing surveys should be a very effective way to characterize the amount of star formation at $z > 7$.

Observers are considering several ways to conduct sur-

veys for $z > 7$ Lyman-α emitters. Before describing the present survey, we therefore consider it instructive to examine the benefits and drawbacks of the different strategies.

The primary survey techniques used thus far are narrowband imaging (Hu et al. 2002, 2004) and spectroscopy (Martin et al. 2006). Neither technique has yet been routinely used in the near-infrared spectral region appropriate for $z > 7$ and both methods can, in principle, be combined with strong lensing by focusing on fields containing rich clusters. At optical wavelengths, unlensed narrow-band imaging techniques typically reach flux limits of 2×10^{-17} ergs cm^{-2} s^{-1}, whereas spectroscopic techniques probe to 5×10^{-18} ergs cm^{-2} s^{-1} (Santos et al. 2004).

In the near-IR, a longslit spectrograph such as NIR-SPEC offers a ~ 8 Å resolution over a moderate redshift interval ($\Delta z = 2$). Although bright atmospheric emission lines restrict visibility for 50% of the redshift range in the J-band, for a resolving power R$\simeq 1500$, the gain in redshift coverage is still a factor of 10-100 over the narrow band technique ($\Delta z = 0.01$-0.1). Per exposure, there is however a very small field of view ($\simeq 30$ arcsec^2) c.f. narrowband imaging ($\simeq 10$ arcmin^2 for a cluster but much larger for panoramic field surveys).

Assuming the characteristics for current instrumentation and their detectors, we compare the efficiencies of the two methods in the lensing case in Figure 1. Details of the computation are given in the Appendix. Both lensed survey techniques probe at least an order of magnitude deeper than conventional near-IR Lyman-α narrowband surveys. Of the two lensing methods, long-slit spectroscopy is better suited for detecting the faintest Lyman-α emitters for detectors 1024$\times$1024 pixels in size. This can be explained as follows. While a narrowband imager covers a larger area on the sky, only a very small fraction of this area is highly magnified (e.g. $>10\times$). The small gain in the highly-magnified survey area is insufficient to compensate for the significantly smaller redshift coverage. Moreover, the $\simeq 100$ Å bandwidth typical for many narrowband filters results in significantly poorer sensitivity limits. Taking the various factors into consideration, a long slit spectroscopic survey represents the more efficient technique for detecting sources with star formation rates below 10^{42} erg s^{-1}, and hence is the optimal strategy for determining whether reionization was predominantly caused by large numbers of feeble sources.

3. NIRSPEC CRITICAL LINE SURVEY

3.1. *Cluster Sample*

Our goal is to constrain the abundance of sources up to an order of magnitude below current survey sensitivity limits. Accordingly, following the discussion above, we have conducted a spectroscopic survey for Lyman-α emission along the critical lines of 9 clusters at $z \simeq 0.2 - 0.5$. We limited our observations to those clusters with mass models that are well-constrained by the combination of HST imaging and ground-based spectroscopy of multiply imaged systems. The list of survey clusters and the associated mass models are summarized in Table 1.

Many criteria entered into the final selection of our 9 clusters. An essential criteria was the availability of deep HST imaging for constructing samples of multiply-imaged systems (Kneib et al. 1996; Broadhurst et al. 2005). The most well-understood clusters in our sample contain 10-30 multiply-imaged systems, a signification fraction of which have spectroscopic redshift (e.g. Abell 1689 has 33 such systems of which 21 are spectroscopically-confirmed, Richard et al, in prep). This data is necessary to astrometrically pinpoint the location of the critical line along which the NIRSPEC slit is oriented.

Deep HST optical imaging is also essential for verifying, via the absence of any detectable continuum, that any lensed emitters are genuinely at high redshift. Due to neutral hydrogen absorption we would not expect any of our $z \simeq 10$ emitters to be seen at optical wavelengths and HST provides the deepest verification.

A final consideration is the availability of deep optical *spectroscopy* which is helpful in order to check for associated emission lines that might arise if any NIR-SPEC line detection arises from a lower redshift source. Given the comprehensive critical line survey undertaken by (Santos et al. 2004) using LRIS, where possible we chose the same clusters and explored the same critical line regions.

In practice, telescope scheduling and weather losses compromised a perfect adoption of the latter criteria. However, for each of the 9 clusters, the mass model, the critical line location and associated magnification properties are well understood.

3.2. *Observations and Data Reduction*

We utilized the Near Infrared Spectrometer (NIR-SPEC, McLean et al. 1998) mounted on the Keck II 10 m telescope at Mauna Kea to perform our survey. Observations were performed in the J-band (1.143-1.375 μm) with a slit $42''$ long and $0.''76$ wide. We used the low-resolution mode of NIRSPEC with the 75 line mm^{-1} grating which offers a net resolving power of R$\simeq 1500$ and a spectral resolution of $\simeq 8$ Å. At the wavelengths sampled within the NIRSPEC J-band filter, any detected Lyman-α emission would correspond to sources with redshifts between $z = 8.5$ and $z = 10.4$.

Figure 2 shows how the targeted slit positions match the predicted location of the $z \simeq 9$ critical lines for each of the 9 clusters in our survey. To maximize efficiency, where a choice was available we selected regions where the critical line is straight enough to provide high magnification across the entire slit.

Typically, 2-5 slit positions were observed per cluster. For each slit position, we took 6-10 ten minute exposures using a three point dither pattern in which the telescope was offset $\pm 3''$ along the slit. Table 2 summarizes the details of our NIRSPEC observations. In four observing runs, we observed 35 slit positions corresponding to a total sky area of 0.3 arcmin^2.

Spectra were flat-fielded and sky-subtracted using IDL scripts written by G. Becker (2004, private communication). Following techniques described in Kelson (2003), the two-dimensional spectra were *not* straightened prior to sky subtraction, thus ensuring sub-pixel sampling of atmospheric emission lines which, in turn, led to a significantly improved removal of the sky background.

The camera distortion and spectral curvature were computed by fitting standard star traces along the slit and atmospheric emission lines across the dispersion axis.

Knowledge of the distortion and spectral curvature was used to construct arrays that provide proxies to the slit position and wavelength for each exposed pixel on the NIRSPEC detector. Using this information, sky background modeling was performed using a two-dimensional b-spline fit, where a low-order polynomial is fit to the slit illumination and a b-spline is fit along the dispersion axis. The wavelength calibration is subsequently computed using atmospheric emission lines. For each exposure, we also compute 2D-variance arrays by summing the contribution from the dark current, flat-field, read noise, sky background, and source counts to the variance.

Following techniques introduced by Santos et al (2004), we determined the astrometric position of each spectral exposure by registering images from the NIRSPEC slit-viewing camera (SCAM) to HST images of the same field. WCS coordinates were computed for each exposed pixel on the detector using the slit position grid described above. Since these are galaxy cluster fields, many bright objects appear in the 46×46 arcsec^2 field of view, enabling accurate registration on to the WCS of the HST images with a typical rms of $0\rlap{.}''15$ (less than 25% of the slit width). Offsets between exposures of a given slit position are calculated from the registered SCAM images, and the 2D-spectra and their associated 2D-variance arrays are subsequently shifted and combined. To remove cosmic rays and bad pixels, we median combine the data rejecting the brightest and faintest frame at each pixel.

Our ability to detect faint emission lines is strongly dependent upon the accuracy with which the offsets between the different exposures of a slit position are known. If a bright emission line from a foreground galaxy lies serendipitously on the slit, the accuracy of the offsets can be determined by comparing the shifts derived from the SCAM images to the offsets between the centroid of the emission line. Suitable emission lines are present in several of our slit positions and applying the aforementioned test, we find the offsets determined from the SCAM images are typically good to $0\rlap{.}''1$. At less than 15% of the slit width, this uncertainty does not compromise the S/N of faint emission features.

One additional concern in dealing with faint emission line objects is the possible transverse drift of the object across the slit from frame to frame when the seeing is less than a slit width (Pelló et al. 2004; Weatherley et al. 2004). This would cause the centroid of the emission line to drift in the *dispersion* direction of the spectrun. Uncorrected, this would increase the area over which the emission line flux is spread, thereby reducing the observed S/N of the emission line in the final stacked spectrum. We quantify the magnitude of the transverse drift by measuring the frame-to-frame centroid of a very bright [OIII] emission line in NIRSPEC observations taken with exceptional seeing ($0\rlap{.}''45$). We find that the standard deviation in the centroid position over 9 frames is 0.8 pixels, or $0\rlap{.}''2$. Adding this measured tranverse drift in quadrature to the seeing FWHM only increases the FWHM of the line by 5%. Given that the seeing was never better than the value quoted above, it is clear that the drift has a negligible effect on the detectability of emission lines.

3.3. *Survey Sensitivity*

We now determine our survey sensitivity function. We first discuss the limiting line flux as a function of wavelength and source redshift. Converting this flux to a limiting source luminosity requires knowledge of the magnification across the NIRSPEC slit. In practice, we will quote our limit in terms of that line flux we can expect to detect, at 5σ confidence, for an unresolved emitter whose rest-frame line width is typical of a faint, but very well-studied, $z \simeq 5.7$ system (Ellis et al. 2001).

To accomplish this, we computed the total noise as a function of dispersion and slit position using the variance arrays obtained in the data reduction (§3.1). This comprises the sum of the variance from the sky background, read noise, flat-fielding, dark count as well as the source counts. Flux calibration of the variance arrays was performed using observations of spectroscopic standard stars. The 5σ limiting Lyman-α line flux was then computed as a function of slit position and wavelength by calculating the signal that is 5 times the root of the variance in an aperture whose spatial dimension is twice the measured seeing disk (typically $0\rlap{.}''7$) and whose spectral dimension equals the Lyman-α line width, ~ 300 km s^{-1} of the lensed system studied with high precision by Ellis et al. (2001).

We find the median 5σ limiting line flux across a typical slit position with 1.5 hours of integration is 2×10^{-17} erg cm^{-2} s^{-1} (see Figure 3); the sensitivity varies between 0.9-3 $\times 10^{-17}$ erg cm^{-2} s^{-1} depending on the proximity to atmospheric OH lines. This flux limit is similar to that reached in the $z = 8.8$ narrowband survey of GOODS-S discussed in Cuby et al. (2006) (1.3×10^{-17} erg cm^{-2} s^{-1}) and slightly less sensitive than the $z = 8.8$ narrowband survey presented in Willis & Courbin (2005) (3.3×10^{-18} erg cm^{-2} s^{-1}); however the lensing magnification enables the detection of sources that are significantly less luminous than those detectable in either conventional narrowband survey.

3.4. *Cluster Magnification*

As discussed in our precursor optical paper (Santos et al. 2004), the cluster mass models listed in Table 1 provide a 2-D map of magnifications for any given source redshift. The details by which these magnifications are realized follow techniques described in detail by (Kneib et al. 1996). Further discussion of the code, LENSTOOL, used to create the mass models for systems for which rich detail is available Jullo et al, (*in prep* and Smith et al. (2005). From each mass model, the magnification can be computed as a function of source redshift and position.

In practice, for each position and wavelength, the mass models produce a matrix of the convergence and shear. The magnification is then determined from the convergence κ and shear γ using the following equation:

$$\mathcal{M}(\boldsymbol{\Omega}, z) = \frac{1}{[1 - \kappa(\boldsymbol{\Omega}, z)]^2 - \gamma(\boldsymbol{\Omega}, z)^2} \qquad (1)$$

where $\boldsymbol{\Omega}$ is the position on the sky and z is the source redshift.

A key question that often arises in the consideration of critical line surveys is the accuracy with which the location of the line can be pinpointed and also that of the associated magnification map. To address this question, we have used a Markov chain Monte Carlo sampling algorithm within LENSTOOL (Jullo et al., in prep) to

map the probability density in the mass model parameter space for each cluster. We then generated a magnification map for each model and in turn computed the mode of the distribution at each pixel as well as the range of magnification factors which bracket the mode by $\pm 34\%$. This we take as the uncertainty in the magnification. The errors derived for each cluster are applied in the determination of both the candidate luminosities (§5) and the survey volume (§6.1).

Taking each exposed pixel on the NIRSPEC detector as an element of solid angle, the convergence and shear is computed as a function of position via interpolation between the NIRSPEC coordinate grid and that of the convergence and shear maps. For each NIRSPEC pixel, the associated redshift at which a Lyman-α emitter would be located is calculated using the wavelength solution described above. The convergence, shear and Lyman-α redshift is then inserted into equation 1 and the magnification $\mathcal{M}$ at each pixel determined. Likewise, the magnification uncertainty map is interpolated onto the NIRSPEC coordinate grid enabling the computation of the error as a function of slit position. Both the magnification and associated error maps were smoothed using a $1''.0$ median box filter to ensure that our results are not corrupted by sharp high peaks in the magnification distribution. The change in the magnification error with redshift is negligible; hence we adopt the uncertainty at $z = 9$ to be the magnification error for all Lyman-α redshifts probed by our survey.

As an example of the magnifications sampled, the wavelength-independent magnification along one of our survey slit positions is displayed in Figure 4 for three different redshifts. The magnification is $> \times 20$ over nearly the entire slit and fairly constant with redshift. We also plot the associated 1σ uncertainty as a function of position along the slit at one of the redshifts. Even allowing for the uncertainty in the lensing model, the magnification is still expected to be uniformly high across the entire slit. This is largely a result of the fact that we only select clusters with well-defined mass models. Furthermore, in regions where the location of the critical line is known less precisely, there is generally a region $\simeq 2''$ in width around the critical line where the magnification factor is greater than fifteen, so the positioning of the NIRSPEC slit is always in a region of high magnification.

Figure 5 presents a histogram of the magnification in our survey. Throughout the entire survey area, the median magnification provided to background sources is $\simeq \times 20$, a factor of two larger than in the optical survey conducted by Santos et al. (2004). The increased magnification is due to several factors. First, ultra-high magnification regions ($\times 15$-30 throughout the slit-area) were preferably selected to allow very low-luminosity systems ($\lesssim 10^{42} ergs^{-1}$) to be probed. Second, since the NIRSPEC longslit covers a factor of three smaller angular extent on the sky than the LRIS longslit used in Santos et al. (2004), we were able to avoid regions where the critical line curved off the slit, resulting in high magnification uniformly across the slit.

3.5. *Limiting Lyman-α Luminosity*

Given our knowledge of the limiting Lyman-α flux (§3.2) and the spatially-dependent magnification (§3.3),

we are now in a position to calculate the limiting source Lyman-α luminosity, $L_{\lim}(\mathbf{\Omega}, z)$. This we define as the least luminous source detectable (with 5σ confidence) in a given volume element, allowing for the cluster magnification $\mathcal{M}$.

Allowing each NIRSPEC pixel to correspond to a volume element, we can calculate the limiting luminosity across each slit in the survey according to the following:

$$L_{\lim}(\mathbf{\Omega}, z) = \frac{4\pi(1+z)^2 D_c^2(z)}{T(\mathbf{\Omega})} \frac{f_{\lim}(z)}{\mathcal{M}(\mathbf{\Omega}, z)}. \qquad (2)$$

where $D_c(z)$ is the comoving distance of the volume element and $T(\mathbf{\Omega})$ is the slit transmission.

In the absence of the lensing magnification, the typical limiting Lyman-α luminosity is $2 \times 10^{43} erg\ s^{-1}$ in between atmospheric OH lines. However, more than 50% of the survey area is magnified by $> \times 30$, enabling the detectability of sources as faint as $7 \times 10^{41} erg\ s^{-1}$ over $\simeq 0.15$ arcmin^2 in the image plane. Conventional narrowband Lyman-α surveys at $z > 6$ typically reach limiting luminosities between 10^{42} and 10^{43} erg s^{-1}. Our NIRSPEC survey probes over an order of magnitude fainter and thus can clearly provide constraints on star forming sources that are otherwise out of reach of traditional methods, at least with current facilities.

4. IDENTIFICATION AND REALITY OF THE CANDIDATE LYMAN-α EMITTERS

At the faint limits now being probed, we have found the reliable identification and verification of distant Lyman-α emitters to be a very challenging endeavor, even with the most powerful facilities available to us. The burden of proof that a detected line is (a) real and (b) truly arises from a highly-redshifted Lyman-α emission line is very great given earlier controversies (Pelló et al. 2004; Bremer et al. 2004; Smith et al. 2006). So far as the identification process is concerned, the key issue is to ensure candidate emission features are not spurious and do not arise from detector artefacts Weatherley et al. (2004). Concerning the redshift verification, a new set of challenges emerge at $z \simeq 10$ since additional (confirmatory) emission lines are not available from ground-based facilities (see §5).

Beginning with the identification process, each of the sky-subtracted 2-D spectra were independently inspected for Lyman-α candidates by three of the authors (D.P.S, R.S.E, and J.R.). We demanded that any candidate feature be both extended over multiple pixels (in order to differentiate a signal from bad pixels and other detector artifacts) and located away from contaminating OH airglow lines. The three lists of line candidates each contained $\simeq 25$ possible features with many being in common between two of the three lists. A final catalog of six promising candidates was constructed by selecting those features with the highest significance common to all three observers. These are displayed in Figure 6. The S/N ratios of these candidate emission lines, defined as in §3.2, varies between 5 and 8 (see Table 3).

A spurious feature could arise if the reduction process does not adequately remove a cosmic ray or bad pixel. Obviously dithering the telescope so the candidates move up and down the slit eliminates most detector anomalies. However artefacts can remain if the spectra are rebinned

during the wavelength calibration; in this case, such bad pixels would be smoothed out and appear similar to emission lines (Weatherley et al. 2004). Fortunately, we do not face this problem in our Keck dataset since our reduction technique altogether avoids rebinning the spectra (see §3). Nevertheless, one may still worry that the measured emission line flux originates from one or two frames with overlapping cosmic rays or bad pixels. We have tested this possibility by median combination of all of the exposures of slit positions containing our candidates and rejecting the three highest pixels. We also median combined half of the exposures (chosen randomly) for each candidate. In both tests, all six candidates are still clearly visible (albeit at lower S/N for the latter test), suggesting that our emission features do not arise from flux in only one or two frames.

Finally, it is conceivable that the noise distribution of the spectral data is such that 5σ noise features are much more common than would be expected under Gaussian statistics. Such a curious situation might arise if there was some unforeseen property of the NIRSPEC detector. In this case our candidate emission features might simply be peaks in the noise distribution. We investigated this possibility by computing the flux in apertures centered at random positions in areas of the spectra where the sky-subtraction is clean. The aperture size was matched to the expected size of a Lyman-α feature at high redshift: the spatial FWHM was taken to be the size of a typical seeing disk, $0''.6$ and spectral FWHM corresponding to typical line width of Lyman-α emitters, 300 km s^{-1})

A normalized histogram of the distribution of summed aperture fluxes is presented in Figure 7. The frequency with which a feature with S/N = 5 appears in our spectra is $\simeq 0.02\%$, which corresponds to just under a 4σ detection for a Gaussian distribution. Though the frequency of features with fluxes comparable to our candidates may be slightly higher than indicated by Gaussian statistics, the test clearly illustrates that features of prominence similar to those of our candidates are extremely rare in clean regions of the spectra.

5. VERIFYING THE CANDIDATE REDSHIFTS

If the emission features discussed above are Lyman-α , then the source redshifts for our 6 candidates range between $z = 8.7$ and $z = 10.2$ and the observed fluxes span 2-5$\times10^{-17}$ erg cm^{-2} s^{-1}. Converting these observed fluxes into intrinsic luminosities is complicated by uncertainties in the fraction of emitted Lyman-α photons that reach the observer. We can compute a lower limit to the unlensed Lyman-α luminosity by converting the fluxes to luminosities and dividing by the magnification factor. With these assumptions, the derived unlensed luminosities range from 1.6-50$\times10^{41}$ erg s^{-1}.

We convert these Lyman-α luminosities to star formation rates assuming case B recombination: $L_\alpha = \frac{2}{3}h\nu_{Ly\alpha}(1 - f_{esc})Q(H)M_\star$ where $h\nu_\alpha$ is the energy of a Lyman-α photon, Q(H) is the Hydrogen ionizing photons flux, and f_{esc} is the fraction of ionizing photons that escape from the galaxy (and hence are not emitted in recombination emission lines). Assuming a Salpeter initial mass function, 1/20th solar metallicity, and a minimum and maximum stellar mass of 1 and 20 M$_\odot$, respectively, the hydrogen ionizing photon flux is 4×10^{53} s^{-1} (Schaerer 2003) for galaxy forming stars continuously at

a rate of 1 M$_\odot$ yr^{-1}. For $f_{esc} \ll 1$ (e.g. Shapley et al. 2006), this results in a conversion factor of 1 M$_\odot$ yr^{-1} = 4.2×10^{42} erg s^{-1}. With these assumptions, the star formation rates range from 0.038 to 1.2 M$_\odot$ yr^{-1}. If a Scalo IMF was adopted instead, the star formation rates would be a factor of three greater (Loeb et al. 2005).

We note that these star formation rates are uncertain for several reasons. If dust in the galaxy absorbs any Lyman-α photons, then the intrinsic luminosities and corresponding star formation rates will be larger. Likewise, if only a fraction of the Lyman-α line is transmitted through the IGM due to the presence of neutral hydrogen, then Lyman-α luminosity and star formation rates will again be underestimated. On the other hand, if the stellar IMF at these early times is more top-heavy than a Salpeter or Scalo IMF, more ionizing photons are predicted per unit of star formation. Similarly, if the metallicity of these galaxies is less than what is assumed above, the efficiency of ionizing photon production (and hence Lyman-α luminosity) is increased (Tumlinson & Shull 2000; Tumlinson et al. 2001; Schaerer 2003). Hence, in these cases, the star formation rates tabulated will be overestimates.

But how can we be sure, with a single emission line, that we have truly detected a Lyman-α emitter? Normally, for a narrow-band imaging survey (Hu et al. 2002, 2004; Malhotra & Rhoads 2004; Shimasaku et al. 2006; Kashikawa et al. 2006) or an unlensed spectroscopic survey (Martin et al. 2006), contamination from foreground [O II] and Hα emitters can be significant. However, it is worth pointing out that such foreground contamination is likely to be much reduced for a critical-line survey designed to probe faint emitters since, for lensing clusters at $z \simeq$0.2-0.5, *all contaminating emitters will also be lensed and thus their respective most-likely location in the image plane will be spatially offset with respect to that for a source at $z \simeq 2$.* The degree to which this benefits a lensed survey with respect to a blank field survey will depend on the relative magnifications at each redshift and the shape of the faint end of the respective line emitting luminosity functions.

A redshift that the general community normally accepts is usually one in which at least two, preferably more, features are reliably identified. Single line identifications are quite naturally questioned as unreliable. As we probe to $z \simeq 10$ with ground-based telescopes, however, we reach the situation where multiple-line identifications are simply not practical. With Lyman-α in the J-band no additional feature is visible in the full practical spectroscopic range from the UV limit to the beginning of the thermally-dominated background at 2μm. The Infrared Spectrograph (*IRS*) on Spitzer in principle offers the possiblity of detecting Hα emission from $z \simeq 10$ objects. However, sensitivity calculations (Lacy et al., in prep.) suggest that the Hα/Lyman-α flux ratio would have to be significantly greater than that expected for case B recombination (perhaps due to Lyman-α suppression from resonant scattering and absorption) in order for this to be an effective verification.

A second-best verification of Lyman-α that might be convincing would be the identification of an associated Lyman break in broadband imaging of the continuum distribution (Stanway et al. 2004) or the presence of an asymmetric line profile (Ellis et al. 2001; Hu et al. 2002).

The Lyman break is due to intergalactic absorption of flux shortward of the Lyman-α line and causes all $z > 7$ sources to be undetected at optical wavelengths. However, the lack of an optical broad-band detection need not necessarily rule out a lower redshift source, for example those with very strong emission line spectra and weak continuum emission.

Asymmetric line profiles are expected because of resonant scattering by neutral hydrogen within the host galaxy and in the IGM. This leads to absorption on the blue side of the line as the light redshifts into resonance, leaving a sharp cutoff on the blue side of the line and an extended red damping wing. Unfortunately, the detection of an asymmetric line profile requires very long integrations and high spectral resolution in order to detect the damping wing.

A key factor in our consideration of how to verify the Lyman-α label for our 6 candidates is the importance of exquisite conditions to see such faint emitters. The required seeing and transparency occur only 40-50% of the time even on an excellent site such as Mauna Kea. Conservatively, we estimated that to measure the Lyman-α profile of any one of our 6 candidates with adequate signal/noise would take 8-10 hours of integration on Keck II. Allowing for weather, to follow-up all 6 candidates in this fashion would take 24 nights; clearly this is not a practical proposition!

One might conclude we have reached new territory where we may never quite know with certainty whether an object is at $z \simeq 10$. In practice, however, there is a way forward although it is less definitive and more statistical in nature. The approach we will adopt is to search spectroscopically in various passbands for lines associated with alternative, lower redshift explanations for the detected J-band emission line. In ruling out a particular alternative identification, we must make some assumptions about the likely emission line spectrum of the interloper. As such this is then a statistical process since we cannot cover all possible emission line ratios. While this method will never confirm the Lyman-α interpretation with 100% certainty, it is clearly an essential prerequisite to spending 2 nights per candidate measuring the line profiles.

In the following subsections, we proceed to apply the tests discussed above to our candidates in order to constrain their redshifts. In §5.1, we examine the stacked line profiles of the six candidates to see if we can collectively assess the likelihood the bulk represent Lyman-α emission; in §5.2, we test for the presence of a Lyman break in deep broadband photometry; finally in §5.3, we discuss our follow-up spectroscopic program to test for low-redshift interlopers.

5.1. *Stacked Line Profile of Candidates*

Asymmetric line profiles cannot be discerned in the individual emission features, because of the low spectral signal/noise. As discussed, much longer integrations (8-10 hrs) would be needed to characterize the emission line profiles and this seems pointless until lower redshift interlopers have been rigorously tested.

Nonetheless, one can ask whether statistically as a combined set, the combined line profile of all 6 candidates reveals an asymmetric profile suggestive of a Lyman-α origin. The practicality of such an exercise is limited by a number of factors. First the resolution of NIRSPEC is only moderate; $R \simeq 1500$ c.f. $R \simeq 15{,}000$ for the ESI spectrum obtained at $z = 5.7$ (Ellis et al. 2001). Second, stacking assumes that all 6 lines are Lyman-α with similar profiles and, most importantly, requires an accurate registration using the central wavelength within each low signal/noise profile. Finally, as the adjacent OH sky lines are distributed differently for each emitter, wavelength regions that are clean in one candidate become averaged with noisy regions in another so the contrast of the stacked line does not increase as $\sqrt{N}$. Even with weighted addition, we did not find the test to be very conclusive.

5.2. *Searching for Lensed Pairs*

In several of the lensed emitters and drop-outs we have published in the past (Ellis et al. 2001; Kneib et al. 2004), the location of a second or third counter-image has been a particularly convincing demonstration of both the lensed hypothesis and, via the mass model, the approximate redshift. Indeed, the accurate recovery of the third image for the $z \simeq 6.8$ drop-out source in Abell 2218 (Kneib et al. 2004) was one of the major arguments justifying its location beyond $z \simeq 6$.

Generally speaking, image pairs are expected in strong lensing configurations depending on the degree of alignment between the background source and the cluster caustics, the physical size of the source and, in this case, the ground-based seeing. The key feature which led to the satisfactory recovery of image pairs in our earlier studies was a broad-band detection with HST. As an example, in the case of the $z = 5.7$ pair discussed by Ellis et al (2001), only a single emitter was recovered by LRIS. The location of the second image required a detection by HST. Indeed, pairs were not detected for any of the other lensed sources in the subsequent LRIS survey (Santos et al. 2004).

Some true pairs may simply not be resolved in our ground-based spectra and, quite possibly, the second image lies outside our NIRSPEC slit coverage. For the most well-constrained mass model, the location of a counter-image can usually be predicted with an uncertainty of $0.\!\!''5$-$1''$, i.e. to within 1-2 NIRSPEC slit widths. Although it is practical to consider chasing the second images, this could still be fairly time-consuming and we concluded that priority should be given in eliminating low-redshift interlopers from our catalog of candidates.

5.3. *Broadband Photometry of Candidates*

The next test is to determine whether optical continuum emission is visible for any of our candidates. Such a detection would clearly rule out a high z interpretation although non-detection does not imply the opposite. Deep ACS/WFPC-2 (Kneib et al. 2004; Smith et al. 2002) images are available for all 9 clusters so we have examined these images at the precise locations of each of our 6 emitters.

No definitive broadband optical detection is seen at the location of any of the candidates to R$\simeq$27.5 (3σ, Figure 8). One of the candidates (Abell 2219 c2) is very marginally detected in the z'_{F850LP}-band; if this flux is associated with the J-band emission feature, then the high redshift interpretation would seem unlikely. Although 3 of the candidates (Abell 2219 c1, Abell 1689

c1, c2) are located within $2\rlap{.}''5$ of brighter objects, in all cases, our registration sufficiently accurate to rule out the possibility that the J-band emission emanates from the bright objects.

A detection in deep near-infrared imaging would be more interesting. Coupled with the optical non-detections discussed above, this might hint at the presence of a Lyman break, lending credence to a $z \simeq 10$ interpretation. In fact, none of the candidates is detected at or above the 5σ level ($\simeq 27$ AB mag) in deep broadband HST J_{110W}, H_{160W} and Keck J-band imaging. Abell 2219 c2 is marginally detected at $\sim 2\sigma$ in the H_{160W}-band.

In fact the lack of definitive near-infrared detections for our Lyman-α candidates is not at all surprising if they are at high-z. If the equivalent width distribution of Lyman-α emitters at $z \simeq 10$ is comparable to that at $z \simeq 4$-6, then we would need to reach $H_{160W} = 27.7$ (1 magnitude below our sensitivity limit) to detect our candidates, if they are indeed Lyman-α emitters (Malhotra & Rhoads 2004; Shimasaku et al. 2006).

Thus, we can conclude that our deep imaging adds a further important component in the case for the hypothesis that bulk of our emission line sources lie at $z \simeq 10$.

5.4. Spectroscopically Testing Low Redshift Scenarios

Aside from Lyman-α, the most likely alternative identifications for the J-band emission features include Hα, [OIII], Hβ, and [OII], in which case the features would correspond to lensed sources at $z = 0.5 - 2.5$. Sources located at these redshifts would almost certainly have additional, associated emission lines bright enough to be seen in the optical and near-infrared spectral regions (see Table 4). We have constrained each of these lower redshift hypotheses by undertaking further spectroscopy, placing stringent limits on the presence of lines.

This technique has value so long as the expected line spectrum of the foreground interlopers is known. In practice selective extinction and excitation differences make the relevant line ratios somewhat uncertain. The best we can do is to approach the problem statistically, assuming a typical HII region spectrum (Figure 9) allowing some leeway in the line ratios.

We generate the HII region spectrum by computing flux ratios of bright recombination lines (Lyman-α, Hα, and Hβ) assuming Case B recombination and accounting for the possibility that a signficant fraction of Lyman-α photons are absorbed by dust thereby reducing its flux by up to a factor of three. With these assumptions, we adopt the following emission line ratios for hydrogen recombination lines: Lyman-α : Hα : Hβ = 7.4-22 : 2.8 : 1.0. Flux ratios involving the forbidden oxygen lines ([OII] and [OIII]) can be determined from observations of low- and high-metallicity galaxies (Pilyugin et al. 2000, 2001). Here we adopt a ratio of [OIII]λ5007 : [OIII]λ4959 : [OII] : Hβ = 0.8-7 : 0.3-2 : 0.8-3 : 1. Using these ratios and the conversion between Lyman-α luminosity and star formation rate (§5), we generate a template spectrum (Figure 9); the continuum flux spectrum is determined for a given star formation rate via a Bruzual & Charlot (2003) model with identical stellar properties to those assumed in §5.

There are certainly a number of shortcomings in such an approach. Predicting the flux of Lyman-α is always difficult due to the resonant nature of the transition. While we allow for a factor of three suppression in the Lyman-α flux, it is possible that a larger fraction of Lyman-α photons could be absorbed. Furthermore, the flux ratios, especially those involving the forbidden oxygen lines, are dependant on the metallicity and the effective temperature of the ionizing stars. However, as we will show below, our observational flux limits are often sufficiently tight to rule out low-redshift hypotheses for a wide variety of metal abundance and stellar effective temperature assumptions.

Following the above logic, after completion of the blind scanning survey, we set out to secure additional optical and H-band spectroscopy for all 6 candidates to apply this interloper-rejection method. Sadly, after two seasons of observing, weather and other observing vagaries mean that exhaustive consideration of all interloper possibilities is only available for 3 of our candidates. For the other 3 candidates, only partial coverage is in place.

Table 4 summarizes the various hypotheses for the J–band emission and lists, for each case, which additional lines would be expected and at what wavelengths. Optical spectroscopy is very efficient at constraining the likelihood that our J-band emission arises from either Hα ($z \simeq 0.9$) or [O III] ($z \simeq 1.5$) since, in these cases, the LRIS data probes very deep in the associated wavelength regions where [O II] would be seen (at 7100 Å and 9300 Å respectively). In some cases, the survey J-band NIRSPEC data can also be used to constrain the hypothesis that the primary detection is $H\beta$ or [O III] where we would expect to locate one or both of the [OIII] λ4959,5007 pair and Hβ. In practice, this is complicated by the fact that lines can be obscured by the OH night sky or seen at very low significance (e.g. 2σ). We found that such cases can be more effectively dispensed with using H-band spectroscopy to search for Hα which should be easily observable if it lies in between the sky lines.

5.5. Best Candidates: Abell 68 c1 and Abell 2219 c1

The most convincing elimination of foreground interloper status has been achieved for the two candidates Abell 68 c1 and Abell 2219 c1. In our subsequent analysis we will assume these emitters are Lyman-α and so we describe these spectroscopic constraints in some detail.

In addition to the null broad-band detections discussed earlier, deep optical LRIS and H-band NIRSPEC spectroscopy was secured in good conditions for both candidates and no definitive features are seen in either case. We summarize the predicted fluxes and limiting sensitivities for each low-redshift interloper case in Table 5.

In the case of Abell 68, if the J-band line was Hα, for our adopted template H II region spectra, [OII] and Hβ would have been recovered with $> 45\sigma$ in the LRIS spectrum.

If the J-band feature was [OII], then Lyman-α would have been seen with ease in the blue LRIS spectrum. While the resonant nature of the transition makes it difficult to predict the Lyman-α flux , if even 0.1% of the photons can escape, a $\simeq 5\sigma$ detection would still have resulted. Since Lyman-α emission is often not seen in distant Lyman break galaxies (Shapley et al. 2003), we can secure additional constraints from the non-detection of Hβ and the two [OIII] lines in the H-band spectrum.

Although some of the relevant regions are affected by OH emission, [OIII] 5007 Å would be strong enough to be detected at $>5\sigma$ under some cases.

If the line were [OIII]λ5007Å , then Hβ, [OIII]λ4959Å , and Hα would all fall in the spectral region covered by the H-band spectroscopy. Hβ and Hα would each be seen at >5 σ for most of the range of emission line ratios.

One seemingly unlikely hypothesis deserves attention. The candidate is quite close (1.8 arcsec) to a $z=1.58$ galaxy with Hβ and [OIII] revealed in the J-band discovery spectrum (Richard et al. 2006, in preparation). If the candidate line were Hβ, the rest-frame velocity separation between the two sources would only be 400 km s^{-1}. The likelihood of an association thus seems high. However, it turns out the combined J+H spectra of the two sources are very different. Hα is seen from the foreground galaxy in the H-band but the same line can be rejected for the candidate with 15σ confidence for a Case B Balmer line ratio. Likewise the limiting sensitivity at the location of [OIII] emission line for the foreground hypothesis is sufficiently deep such that we would have expected to see a line for nearly all reasonable line ratio assumptions. In combination, therefore, the non-detection of Hα and [OIII]λ 5007 Å strongly rule out any association of the candidate with the z=1.58 galaxy.

Similarly, in the case of Abell 2219 c1 if the J-band line were Hα, [OII], Hβ and [O III] 4959Å would have been seen in the LRIS spectra at 23-85, 8.5, and 6.4-43 σ respectively.

If the line was Hβ, Hα would have been detected at 22σ in the H-band spectrum.and [OIII] λ4959Å and λ5007Å at 3.5-24 and 21-190 σ respectively in the J-band.

If the line were [OII], then, as before strong Lyman-α would be expected in the blue LRIS spectrum, even if only a small fraction of photons escaped. And [OIII]λ4959Å and λ5007Å would have been seen at up to 4.5-8.0 and 4.8-11σ respectively in the H-band spectrum.

Finally, if the line were [OIII] λ5007Å , then Hβ would be detected at $1.7-15\sigma$, depending on the oxygen abundance. and Hα would been seen in a clean area of the H-band with 4.8-43σ.

All cases described above assume an HII region template spectrum. Assuming the emission lines are instead generated by a harder ionization source such as an AGN, the CIV $\lambda\lambda$ 1548, 1550 line may be prominent in the rest-frame UV spectrum. If Lyman-α is suppressed via resonant scattering and absorption by dust, narrow-line AGN can exhibit line ratios of $1\lesssim$ CIV/Lyα $\lesssim$ 1.4 (Dey et al. 1995; De Breuck et al. 2001; Dawson et al. 2003). If these sources are indeed Lyman-α emitters at $z \simeq 10$, then the CIV line may also be observable in the H-band. For both Abell 68 c1 and Abell 2219 c1, CIV would lie in clean regions (1.60 μm and 1.55 μm, respectively); however, neither emission line is seen, suggesting that if the candidates are at $z \simeq 10$, they have CIV/Lyα < 1.

5.6. *Other Candidates*

Comprehensive optical and H-band spectroscopy is also available for Abell 2219 c2 and in fact the constraints we discuss above for Abell 2219 c1 are just as convincing

here making it a very promising source. However, we prefer not to elevate it into the status of the two most promising sources because of the potential broad-band ACS detection (§5.2). In this sense it represents a source of status intermediate between our top two candidates and those discussed below for which, due to weather and other problems, our spectroscopy is currently incomplete.

For A1689c1, c2 and c3, we have no optical or H-band spectroscopy and so major interloper hypotheses such as $H\alpha$ and [O II] cannot yet be excluded.

In summary, we can conclude that at least two (and quite possibly three) of our six candidates cannot be accounted for as lines from lower redshift emitters. Moreover, there is no reason to denigrate the status of the other 3 candidates either since, so far, every additional spectrum we have taken has continued to support the Lyman-α hypothesis. Our low contamination ratio is not that surprising when one considers all of the considered interloper hypotheses would still represent lensed systems and thus, if highly magnified, not be seen at the location of the $z \simeq 10$ critical line.

On the other hand, it is clear that our tests make necessary assumptions about the line ratios expected from $0.85 < z < 2.26$ galaxies. It is conceivable that these assumptions are invalid and that the sources have anomalous line ratios (although it would seem surprising that this is the case in several systems). Given the wavelength ranges accessible to ground-based spectrographs, we believe we have undertaken all possible tests.

6. IMPLICATIONS

Noting that at least two of our six candidates may indeed lie at $z \simeq 10$, we now address the goal of the survey: what is the volume density of high z emitters? However, noting their identification could still be considered tentative, we will also explore the implications if *none* of our candidates is real. After making simple assumptions about the effect of dust and resonant scattering on escaping Lyman-α photons, we will use the derived abundance to constrain the star formation rate density. We then attempt to understand whether the derived abundance represents a significant contribution to the ionizing photon budget at $z \simeq 10$.

6.1. *Volume Density of z>8 Lyman-α Emitters*

In a blank-field survey, the surface density of sources brighter than a given limiting line flux can be computed by dividing the number of detected sources by the area observed. The calculation is more complex in this case because of the varying amplification of the source flux over the survey volume and the distortion, by lensing, of the survey area.

The differential comoving volume element at $(\mathbf{\Omega},z)$ along one of the NIRSPEC slit positions is

$$dV_c(\mathbf{\Omega}, z) = \frac{1}{\mathcal{M}(\mathbf{\Omega}, z)} \left[\frac{dl_c(z)}{dz} dz \right] \times \left[D_c^2(z) d\mathbf{\Omega} \right]. \quad (3)$$

where dl_c is the comoving length of the volume element along the line of sight. We also compute the uncertainty associated with each volume element due to the error in the magnification (§3.4).

The total survey volume over which sources with Lyman-α line luminosity greater than L is the integral

over all volume elements with limiting Lyman-α luminosity below L,

$$V_c(L) = \int_{\boldsymbol{\Omega}} \int_z dV_c(\boldsymbol{\Omega}, z) \; H[L - L_{\lim}(\boldsymbol{\Omega}, z)], \quad (4)$$

where H[L-$L_{\lim}(\boldsymbol{\Omega}, z)$] is a step function equal to 1 when L$\geq L_{\lim}(\boldsymbol{\Omega}, z)$ and equal to 0 when L$< L_{\lim}(\boldsymbol{\Omega}, z)$.

The uncertainty in the magnification introduces error into the derived comoving volume. We quantify this error by computing the distribution of comoving volume for all acceptable cluster mass models (see § 3.4). The range of comoving volume that spans $\pm 34\%$ of the total samples is taken to be the uncertainty in the volume.

The survey volume and associated errors are plotted as a function of Lyman-α luminosity in Figure 10. The comoving volume decreases from $\simeq 30$ Mpc^3 at L=3$\times 10^{42}$ erg s^{-1} to $\simeq 3$ Mpc^3 at L=3$\times 10^{41}$ erg s^{-1}. The 'one-sigma' error bars in the volume are small enough that they do not extend outside the datapoints. In Figure 11, we plot the number density of $z \simeq 9$ Lyman-α emitters as a function of Lyman-α luminosity assuming that (i) none of our candidates is at $z \simeq 8$-10 (left) and (ii) two of our candidates are Lyman-α emitters (middle) and (iii) all six of our candidates are real (right).

In the case where two of the candidates are real, the Poisson errors are 100%. This arises because galaxies need not only be brighter than the survey limiting luminosity but must also lie within the area covered by the survey. In lensing experiments, in order for inclusion associated with some limiting luminosity, the 5σ limiting luminosity at the location of the object must be lower than the limiting luminosity of the survey. The net result is that objects with fluxes close to the sensitivity limits only are included in "surveys" with a small range of limiting luminosities. If two candidates are real, as considered here, the luminosity ranges over which the objects would be detected do not overlap; hence no bin contains more than one object.

To place the inferred abundances in context, we compare our results with other surveys that have been conducted, particularly at z$\simeq 6$ where the luminosity function of Lyman-α emitters is more firmly established.

The first observational constraint on the abundance of Lyman-α emitters at z>8 was presented by (Willis & Courbin 2005). These authors conducted a narrow-band imaging survey in the J-band toward the Hubble Deep Field South and found no $z = 8.8$ sources with Lyman-α luminosity greater than $10^{42.5}$ erg s^{-1} over a volume of approximately 990 Mpc^{-3}. More recently, Cuby et al. (2006) reported a null detection of $z = 8.8$ Lyman-α emitters brighter than 10^{43} erg s^{-1} over a comoving volume of $\simeq 4200 Mpc^3$. Given the large error bars, the upper limits from Willis & Courbin (2005) and Cuby et al. (2006) are consistent with the case in which only two of the candidates are real. If all six of the candidates are Lyman-α emitters, it becomes slightly more difficult to explain the lack of Lyman-α emitters in the two narrowband surveys without resorting to luminosity dependent evolution. Hence, in this case, the observations could suggest that the decline in luminous Lyman-α emitters relative to fainter sources observed at $z \simeq 6-7$ (Shimasaku et al. 2006; Kashikawa et al. 2006; Iye et al. 2006) continues to $z \simeq 10$.

A second question is whether our density is higher or lower than the Lyman-α luminosity function which is now fairly well-established at $z = 5.7$, at least at the bright end (Santos et al. 2004; Malhotra & Rhoads 2004; Shimasaku et al. 2006). It is worth remembering that despite the fact that over 100 Lyman-α emitters are now catalogued at this redshift, the degree of spectroscopic confirmation is still quite limited. The extant data are well-fit by a Schechter function with $\phi^\star = 1.6 \times 10^{-4}$ Mpc^{-3} and L$^\star = 1.6 \times 10^{43}$ erg s^{-1} where, for the purposes of discussion, we have adopted the steepest likely faint-end slope of $\alpha = -2$ so as to provide the most optimisitc no-evolution scenario. Assuming, naively, no evolution between z=5.7 and z=10, it is unlikely that we would find a source brighter than 10^{40} erg s^{-1}. At face value, therefore, our detection of at least two promising cases would suggest an upwards evolution in the abundance of faint emitters with redshift.

The likely evolution of the Lyman-α luminosity function between z=5.7 and z$\simeq 10$ is a complicated function of the star formation efficiency, stellar initial mass function, relative geometry and kinematics of HII and HI gas, and dust content of the host galaxy, as well as the ionization state of the IGM. If, for example, the dust content of galaxies decreases toward higher redshifts, the percentage of Lyman-α photons that escape the host galaxy may increase. On the other hand, as the IGM becomes increasingly neutral, observed Lyman-α counts are expected to decline (Malhotra & Rhoads 2004; Haiman & Cen 2005), although the presence of large HII regions around clustered star-forming sources may slightly offset the magnitude of this decline (Furlanetto et al. 2004). Clearly, it is very difficult to predict exactly *how* the Lyman-α luminosity function will evolve over this $\simeq 500$ Myr time interval.

Bearing these uncertainties in mind, our detection of two promising candidates clearly implies a steep faint-end slope and hence a large abundance of intrinisically faint sources. If more of our candidates are at $z \simeq 10$, it would almost certainly imply that low-luminosity star-forming systems are *more* abundant at $z = 9$ than at $z = 5.7$. This may be a result of evolution in galaxy properties (as discussed), or the effect of a predominantly neutral IGM which increases star formation efficiency in low-mass halos due to the decrease in the Jeans mass (Barkana & Loeb 2001). Determining which of these factors is primarily responsible for the possible upturn in counts is difficult with the available data.

If none of our candidates is real, a number of explanations are possible. First the faint-end slope may not be as steep as required for us to detect sources in our observed volume. There are a number of feedback processes (galactic winds, supernova explosiona, etc.) that could significantly reduce star formation efficiency in low-mass halos, thereby resulting in a relatively shallow faint-end slope. Alternatively, if the IGM is significantly neutral, it is possible that faint-end slope is very steep, but the neutral IGM is blocks our view of these systems. We defer a detailed discussion of the implications of our survey in terms of what is now known at $z \simeq 5$-6 to a later paper (Stark, Loeb & Ellis, 2007).

6.2. *Contribution of Low Luminosity Galaxies to Reionization*

Several methods have been adopted for considering the contribution of star-forming sources to cosmic reionization. One approach is to compare the inferred ionizing photon production rate from star-forming galaxies of all luminosities to that required to reionize neutral hydrogen in the IGM (Madau et al. 1999; Stiavelli et al. 2004). Since the abundance of Lyman-α emitters at $z \simeq 10$ is very uncertain, comparing the total ionizing photon output is highly dependent upon assumptions about the luminosity function. In this initial study, we ask a more basic question: do low luminosity Lyman-α emitters provide a significant contribution to reionization? Following this approach, we therefore only tabulate the ionizing photon production arising from low luminosity (i.e. 10^{41} - 10^{42} erg s^{-1}) sources that our survey is designed to probe.

The contribution of low luminosity star-forming sources to reionization can be parameterized in simple terms by comparing their ionizing photon production rate to that required for reionization:

$$n_{\mathrm{gal}} = 2 \left(\frac{\mathrm{B}}{10}\right)\left(\frac{\mathrm{f}_{\mathrm{esc}}}{0.05}\right)^{-1}\left(\frac{\dot{\mathrm{M}}_{\star}}{0.1 \; \mathrm{M}_{\odot} \; \mathrm{yr}^{-1}}\right)^{-1}$$
$$\left(\frac{\Delta \mathrm{t}}{575 \; \mathrm{Myr}}\right)^{-1} \mathrm{Mpc}^{-3} \qquad (5)$$

assuming the space density of sources is constant during the reionization epoch. Here, B is the number of ionizing photons required to keep a single hydrogen atom ionized, n_{H} is the comoving number density of hydrogen at the redshift of interest, $\Delta \mathrm{t}$ is the period over which reionization occurs, f_{esc} is the escape fraction of ionizing photons, $\dot{\mathrm{M}}_{\star}$ is the time-averaged star formation rate of galaxies in units of $\mathrm{M}_{\odot} \; \mathrm{yr}^{-1}$.

In both cases, we fix the comoving number density of hydrogen at $n_{\mathrm{H}} = 1.9 \times 10^{-7}$ cm^{-3}, appropriate for the comoving hydrogen number density adopting the best-fit WMAP cosmological parameters (Spergel et al. 2006). We have also assumed an IMF with Salpeter slope with stellar masses ranging from 1 $\mathrm{M}_{\odot}$ to 100 $\mathrm{M}_{\odot}$ and metallicity of of Z=0.001 (1/20th solar) (Schaerer 2003). If the IMF is weighted more toward massive stars or is substantially more metal-poor, the ionizing photon output for a given star formation rate will be greater, and less galaxies will be required for reionization.

The escape fraction of ionizing photons is not well-constrained observationally; we allow this quantity to vary between 0.02 and 0.5 (Steidel et al. 2001; Fernández-Soto et al. 2003; Shapley et al. 2006). We assume the escape fraction is constant with luminosity; however, models of high-redshift galaxies suggest that it should increase toward the low-luminosity end of the luminosity function (Ricotti & Shull 2000). If this is the case, then contribution of low-mass galaxies to reionization will be even greater than what is shown below.

The recombination rate increases with the local hydrogen number density, hence the number of ionizations required per atom for reionization depends strongly on the clumpiness of the IGM ($\mathrm{C} = \frac{\langle n_e^2 \rangle}{\langle n_e \rangle^2}$). Simulations generally predict clumpiness factors of C$\sim$30 (Gnedin 2000) for z$\sim$6-7. Following the interpolation formulae

in (Stiavelli et al. 2004), this results in $\simeq$5-10 ionizations per hydrogen atom depending on the timescale of reionization.

Substituting the range of parameter values into equation 5, we find that for galaxies with star formation rates of 0.1 $\mathrm{M}_{\odot}$ yr^{-1} to dominate the reionization process, they should have comoving number densities in excess of 0.1 - 4 Mpc^{-3} (Figure 12). If two or more of the candidates are at z$\simeq$10, then it would appear that low luminosity galaxies contribute significantly to the reionization process.

While there is currently not enough data at $z \simeq 10$ to estimate the integrated ionizing photon output from Lyman-α emitters, we can attempt to constrain this quantity by assuming that the luminosity function evolves only in normalization (hence maintaining the same shape) between $z = 6.5$ and $z = 10$. In the most optimistic case where six candidates are at high-redshift, we take the characteristic luminosity, L* derived for the $z = 6.5$ Lyman-α emitters by Kashikawa et al. (2006) with a diverging faint-end slope of $\alpha = -2$. Integrating the luminosity function down to the survey limit ($\simeq$0.01 $\mathrm{M}_{\odot}$ yr^{-1}), we find that the total ionizing photon production rate would be sufficient for reionization for nearly the full range of assumptions considered in Figure 12.

7. SUMMARY

Low luminosity star-forming galaxies are often predicted to produce a large supply of ionizing photons during the reionization era (Barkana & Loeb 2001). However, feedback processes from supernova explosions or galaxy winds may significantly decrease star formation efficiency in the low-mass dark matter halos that are thought to house the majority of low-luminosity star forming sources. Tentative observational evidence hints at a very large abundance of low luminosity sources (Yan & Windhorst 2004; Bouwens et al. 2006) suggesting that these feedback processes may not significantly affect star formation in low-mass halos. Until the construction of JWST and 20-40 meter class ground-based telescopes, gravitational lensing surveys offer one of the most efficient means of spectroscopically verifying the presence of an abundant population of low-luminosity ($\lesssim 10^{43}$ergs^{-1}) sources. With this as our goal, we have conducted a spectroscopic survey for gravitationally lensed Lyman-α emitters over the redshift interval $8.5 < z < 10.4$. We summarize our results below.

1. The critical lines of 9 well-understood lensing clusters were scanned spectroscopically in the J-band for lensed Lyman-α emission from galaxies at z=8.5 to 10.4. The new observations are sensitive to star-forming sources with intrinsic (unlensed) Lyman-α luminosities of $10^{41.5}$ erg s^{-1} over a significant fraction of the survey area. This limit is over an order of magnitude fainter than the corresponding sensitivity limits of conventional surveys for Lyman-α emitters at $z > 6$.

2. Six promising candidate Lyman-α emitters were identified whose reality we justify noting the possibility of instrumental and detector artefacts. The emission features have fluxes that range from 2-5$\times 10^{-17}$ erg cm^{-2} s^{-1} and significances between 5-8σ. The Lyman-α luminosities of the sources range from 10^{41} to 5×10^{42} erg s^{-1}.

3. We attempt to verify that our lines arise from $z \simeq 10$

Lyman α via several tests. No convincing broadband optical counterparts were seen in deep HST images (R$\simeq$27) except in one marginal case. For 3 out of the 6 cases, we conduct exhaustive additional spectroscopy to explore the likelihood that low-redshift interloper lines may explain the J-band emission. In no case do we find such an example, and, overall we conclude that at least 2 of our 6 candidates probably lie at $z \simeq 10$. We briefly discuss the considerable challenges of making further progress in confirming any or all of our candidates given the limited rest-wavelength range available with large ground-based telescopes.

4. Assuming two or more of our Lyman-α emitter candidates are real, then the cumulative abundance of low luminosity galaxies (defined as those with L$>10^{41.5}$ erg s^{-1}) is at least 0.3 Mpc^{-3}. Such a large abundance of low luminosity Lyman-α emitters supports the contention of a steep faint end slope for the star-forming luminosity function at z$\simeq$10.

5. Assuming a single population of galaxies dominates the reionization process the number density of galaxies forming stars at a rate of 0.1 M$_\odot$ yr^{-1} must exceed 0.1-4 Mpc^{-3} to reionize neutral hydrogen. Our inferred abundance is consistent with being within this range indicating that intrinsically faint Lyman-α emitters may well produce a substantial supply of ionizing photons during the reionization era.

6. However, if none of our candidates are at high-redshift, then there are several likely explanations. If the IGM is significantly neutral, low luminosity star forming systems may be very abundant but may not be observed due to resonant absorption of Lyman-α photons by hydrogen in the IGM. Alternatively, it is possible that the faint-end slope is not as steep as predicted by Yan & Windhorst (2004); hence larger volumes would be needed to detect a representative sample.

Notwithstanding the uncertainties and speculation, our survey demonstrates the practicality, over the next few years, of providing a valuable glimpse at the nature of the $z \simeq 10$ Universe ahead of the commissioning of future large facilities such as the Thirty Meter Telescope and the James Webb Space Telescope.

<div style="text-align:center">REFERENCES</div>

Barkana, R., & Loeb, A. 2001, Phys. Rep., 349, 125
Beckwith, S. V. W., et al. 2006, AJ, 132, 1729
Bézecourt, J., Kneib, J. P., Soucail, G., & Ebbels, T. M. D. 1999, A&A, 347, 21
Borys, C., et al. 2004, MNRAS, 352, 759
Bouwens, R. J., & Illingworth, G. D. 2006, Nature, 443, 189
Bouwens, R. J., Illingworth, G. D., Blakeslee, J., & Franx, M. 2006, ApJ,submitted
Bouwens, R. J., Illingworth, G. D., Thompson, R. I., & Franx, M. 2005, ApJ, 624, L5
Bremer, M. N., Jensen, J. B., Lehnert, M. D., Schreiber, N. M. F., & Douglas, L. 2004, ApJ, 615, L1
Broadhurst, T., et al. 2005, ApJ, 621, 53
Bruzual, G., & Charlot, S. 2003, MNRAS, 344, 1000
Cuby, J. ., Hibon, P., Lidman, C., Le Fevre, O., Gilmozzi, R., Moorwood, A., & van der Werf, P. 2006, Accepted for publication in A&A, astro-ph/0611272
Dawson, S., McCrady, N., Stern, D., Eckart, M. E., Spinrad, H., Liu, M. C., & Graham, J. R. 2003, AJ, 125, 1236
De Breuck, C., et al. 2001, AJ, 121, 1241
Dey, A., Spinrad, H., & Dickinson, M. 1995, ApJ, 440, 515
Ebbels, T., Ellis, R., Kneib, J.-P., Leborgne, J.-F., Pello, R., Smail, I., & Sanahuja, B. 1998, MNRAS, 295, 75
Ebeling, H., Edge, A. C., & Henry, J. P. 2001, ApJ, 553, 668
Egami, E., et al. 2005, ApJ, 618, L5
Ellis, R., Santos, M. R., Kneib, J.-P., & Kuijken, K. 2001, ApJ, 560, L119
Eyles, L. P., Bunker, A. J., Ellis, R. S., Lacy, M., Stanway, E. R., Stark, D. P., & Chiu, K. 2006, MNRAS, 1348
Eyles, L. P., Bunker, A. J., Stanway, E. R., Lacy, M., Ellis, R. S., & Doherty, M. 2005, MNRAS, 364, 443
Fan, X., et al. 2006, AJ, 132, 117
Fernández-Soto, A., Lanzetta, K. M., & Chen, H.-W. 2003, MNRAS, 342, 1215
Furlanetto, S. R., Zaldarriaga, M., & Hernquist, L. 2004, ApJ, 613, 1
Gnedin, N. Y. 2000, ApJ, 542, 535

Haiman, Z., & Cen, R. 2005, ApJ, 623, 627
Henry, A. L., Malkan, M. A., Colbert, J. W., Siana, B., Teplitz, H. I., McCarthy, P., & Yan, L. 2007, Accepted to ApJ Letters, astro-ph/0701045
Horton, A., Parry, I., Bland-Hawthorn, J., Cianci, S., King, D., McMahon, R., & Medlen, S. 2004, in Ground-based Instrumentation for Astronomy. Edited by Alan F. M. Moorwood and Iye Masanori. Proceedings of the SPIE, Volume 5492, pp. 1022-1032 (2004)., ed. A. F. M. Moorwood & M. Iye, 1022
Hu, E. M., Cowie, L. L., Capak, P., & Kakazu, Y. 2005, in IAU Colloq. 199: Probing Galaxies through Quasar Absorption Lines, ed. P. Williams, C.-G. Shu, & B. Menard, 363
Hu, E. M., Cowie, L. L., Capak, P., McMahon, R. G., Hayashino, T., & Komiyama, Y. 2004, AJ, 127, 563
Hu, E. M., Cowie, L. L., & McMahon, R. G. 1998, ApJ, 502, L99
Hu, E. M., Cowie, L. L., McMahon, R. G., Capak, P., Iwamuro, F., Kneib, J.-P., Maihara, T., & Motohara, K. 2002, ApJ, 568, L75
Iye, M., et al. 2006, Nature, 443, 186
Kashikawa, N., et al. 2006, ApJ, 648, 7
Kelson, D. D. 2003, PASP, 115, 688
Kneib, J.-P., Ellis, R. S., Santos, M. R., & Richard, J. 2004, ApJ, 607, 697
Kneib, J.-P., Ellis, R. S., Smail, I., Couch, W. J., & Sharples, R. M. 1996, ApJ, 471, 643
Kneib, J.-P., et al. 2003, ApJ, 598, 804
Labbé, I., Bouwens, R., Illingworth, G. D., & Franx, M. 2006, ApJ, 649, L67
Loeb, A., Barkana, R., & Hernquist, L. 2005, ApJ, 620, 553
Lord, S. 1992, NASA Tech. Rep. 103957
Madau, P., Haardt, F., & Rees, M. J. 1999, ApJ, 514, 648
Malhotra, S., & Rhoads, J. E. 2004, ApJ, 617, L5
Martin, C. L., Sawicki, M., Dressler, A., & McCarthy, P. J. 2006, New Astronomy Review, 50, 53
McLean, I. S., et al. 1998, in Proc. SPIE Vol. 3354, p. 566-578, Infrared Astronomical Instrumentation, Albert M. Fowler; Ed., ed. A. M. Fowler, 566

Mobasher, B., et al. 2005, ApJ, 635, 832

Pelló, R., Schaerer, D., Richard, J., Le Borgne, J.-F., & Kneib, J.-P. 2004, A&A, 416, L35

Richard, J., Pelló, R., Schaerer, D., Le Borgne, J.-F., & Kneib, J.-P. 2006, A&A, 456, 861

Ricotti, M., & Shull, J. M. 2000, ApJ, 542, 548

Santos, M. R., Ellis, R. S., Kneib, J.-P., Richard, J., & Kuijken, K. 2004, ApJ, 606, 683

Schaerer, D. 2003, A&A, 397, 527

Shapley, A. E., Steidel, C. C., Pettini, M., & Adelberger, K. L. 2003, ApJ, 588, 65

Shapley, A. E., Steidel, C. C., Pettini, M., Adelberger, K. L., & Erb, D. K. 2006, ApJ, 651, 688

Shimasaku, K., et al. 2006, PASJ, 58, 313

Smith, G. P., Kneib, J.-P., Smail, I., Mazzotta, P., Ebeling, H., & Czoske, O. 2005, MNRAS, 359, 417

Smith, G. P., Sand, D. J., Egami, E., Stern, D., & Eisenhardt, P. R. 2006, ApJ, 636, 575

Smith, G. P., et al. 2002, MNRAS, 330, 1

Spergel, D. N., et al. 2006, ApJ,submitted

Spergel, D. N., et al. 2003, ApJS, 148, 175

Stanway, E. R., Bunker, A. J., McMahon, R. G., Ellis, R. S., Treu, T., & McCarthy, P. J. 2004, ApJ, 607, 704

Stark, D. P., Bunker, A. J., Ellis, R. S., Eyles, L. P., & Lacy, M. 2006, Accepted in ApJ, astro-ph/0604250

Steidel, C. C., Pettini, M., & Adelberger, K. L. 2001, ApJ, 546, 665

Stern, D., Yost, S. A., Eckart, M. E., Harrison, F. A., Helfand, D. J., Djorgovski, S. G., Malhotra, S., & Rhoads, J. E. 2005, ApJ, 619, 12

Stiavelli, M., Fall, S. M., & Panagia, N. 2004, ApJ, 600, 508

Swinbank, A. M., Bower, R. G., Smith, G. P., Smail, I., Kneib, J.-P., Ellis, R. S., Stark, D. P., & Bunker, A. J. 2006, MNRAS, 368, 1631

Totani, T., Kawai, N., Kosugi, G., Aoki, K., Yamada, T., Iye, M., Ohta, K., & Hattori, T. 2006, PASJ, 58, 485

Tumlinson, J., Giroux, M. L., & Shull, J. M. 2001, ApJ, 550, L1

Tumlinson, J., & Shull, J. M. 2000, ApJ, 528, L65

Weatherley, S. J., Warren, S. J., & Babbedge, T. S. R. 2004, A&A, 428, L29

Willis, J. P., & Courbin, F. 2005, MNRAS, 357, 1348

Wyithe, J. S. B., & Loeb, A. 2006, Nature, 441, 322

Yan, H., Dickinson, M., Giavalisco, M., Stern, D., Eisenhardt, P. R. M., & Ferguson, H. C. 2006, ApJ, 651, 24

Yan, H., et al. 2005, ApJ, 634, 109

Yan, H., & Windhorst, R. A. 2004, ApJ, 600, L1

APPENDIX

The observing sequence for narrowband surveys often involves alternating between two narrowband filters (e.g. A and B) with slightly different central wavelengths. In each filter, the observations are divided into subexposures with integration times that are comparable to the variability timescale of the sky background (typically 5-10 minutes). A composite image is made of all of the subexposures in each filter, resulting in two "subsurveys" slightly offset in redshift space. Subtracting the two composite images removes continuum soures, thereby allowing line emitters to be identified. Alternatively, instead of a second narrowband filter, a broadband filter can be used to identify line emitters (Willis & Courbin 2005). Using either approach, if integration time t_{int} is devoted to a narrowband survey, then the total integration devoted to each individual "subsurvey" is only ($t_{int}/2$) in length. In the following calculations, we assume a total integration time of 60 hours.

The field of view of the survey camera is one of the key parameters in determining the survey sensitivity. For a single exposure, the field of view is limited by the size of the detector and the plate scale of the detector. The plate scale is typically set such that each pixel samples 1/4 of a spatial resolution element. Assuming seeing-limited observations with a $0\rlap.{''}6$ seeing disk, this corresponds to 0.1-0.2 arcseconds per pixel. Until very recently, only 1024×1024 pixel detectors were available on 8-10 meter telescopes in the near-infrared; given typical plate scales, this allows fields of view between 3 and 12 arcmin^2. Recently, larger format cameras have become available (e.g. MOIRCS on Subaru) allowing fields of view of $\simeq$30 arcmin^2 to be observed in single exposures. In the signal to noise calculations that follow, we consider both a detector with a field of view of 4 arcmin^2 (similar to that of NIRI on Gemini) as well as one with a field of view of 30 arcmin^2.

In the near-infrared, the noise is dominated by bright atmospheric emission lines from OH molecules; hence the background in a given exposure is dependent on the central wavelength and bandwidth of the narrowband filter. The central wavelength is chosen to lie in >50Å gaps between bright OH lines, where the atmospheric transmission is near 100%. We assume a central wavelength of 11905 Å for our predictions. The signal to noise in a single exposure is minimized when the filter bandwidth is matched to the FWHM of the emission line, which is typically 5-10 Å for Lyman-α emitters at high redshift (Shimasaku et al. 2006); hence, we adopt 10Å as the FWHM for our calculations. We also consider a filter with a FWHM of 100 Å; while the noise in a single exposure is larger for this filter, the redshift range covered is ten times larger (Δz=0.1 vs. Δz=0.01).

The received signal from the science source is estimated as follows,

$$S_{source} = \int f_{\lambda,source}\tau(\lambda)\,d\lambda\ A_{tel}\eta_{tel}\eta_{inst}\eta_{QE}\eta_{atm}(t_{int}/2) \qquad (A-1)$$

where $f_{\lambda,source}$ is the spectrum of the source in units of photons s^{-1} cm^{-2} Å^{-1}, $\tau(\lambda)$ is the filter transmission profile (assumed gaussian with FWHM defined above), η_{tel} is the telescope optics throughput, η_{inst} is the throughput of the instrument, η_{QE} is the quantum efficiency of the detector, η_{atm} is the atmospheric transmision, A_{tel} is the collecting area of the telescope. As discussed in §5.1, we expect the line profile of high-redshift Lyman-α emitters to be asymmetric with the blue side of the line absorbed. Along these lines, we assume the line profile is a half-Gaussian with no flux shortward of the central wavelength. While this profile is perhaps oversimplified, the S/N calculations do not change signficantly if the profile is altered. We adopt throughput and quantum efficiency values that are consistent with those expected for DAzLE (η_{tel}=0.6, η_{inst}=0.5, η_{QE}=0.7), a near infrared narrowband imager designed to find $z > 7$ Lyman-α emitters Horton et al. (2004). The atmospheric transmission, η_{atm}, is computed following models presented in Lord (1992) assuming an air mass of 1.5 and a 1.0 mm water vapour column [5] and is near unity for the OH window considered. We assume a telescope collecting area of 7.9×10^5 cm^2 corresponding to the size of Keck. The photometric aperture is matched to the area subtended under reasonably good seeing conditions ($\simeq 0\rlap.{''}6$ diameter seeing disk). The integration time is only ($t_{int}/2$) because the total integration time is split between two different narrowband filters, as described above.

The noise in an exposure of time t_{int} is a function of the integrated source counts, sky background, detector dark current, and detector read noise. Formally, the noise is defined as

$$N = \sqrt{N_{sky} + N_{source} + N_{DC} + RN^2} \qquad (A-2)$$

where N_{sky}, N_{source}, N_{DC} are the number of electrons from the sky background, science source, and dark current, and RN is the read noise.

We compute the expected background count rate utilizing the Gemini model for the near-infrared sky background spectrum[6]. The model inludes the contribution from atmospheric OH emission lines, zodiacal emission (from a 5800 K blackbody), and thermal emission from the atmosphere (from a 250 K blackbody). The total counts from the sky background in a photometric aperture of area a_{phot} in the composite image, is given by

$$N_{sky} = \int f_{\lambda,sky}\ \tau(\lambda)\,d\lambda\ \eta_{tel}\eta_{inst}\eta_{QE}\ A_{tel}\ a_{phot}\ (t_{int}/2) \qquad (A-3)$$

where $f_{\lambda,sky}$ is the sky background in photons s^{-1} cm^{-2} Å^{-1} arcsec^{-2}, τ is the filter transmission profile (assumed gaussian with FWHM defined above), a_{phot} has units of arcsec^2, and all other parameters are the same as defined above.

---

[5] available from `http://www.gemini.edu/sciops/ObsProcess/obsConstraints/atm-models/trans_10_15.dat`
[6] available from `http://www.gemini.edu/sciops/ObsProcess/obsConstraints/atm-models/nearIR_skybg_16_15.dat`

TABLE 1
CLUSTERS SURVEYED

Cluster	Redshift	RA[a]	Dec[b]	Lens Model Reference
Cl 0024	0.39	00 26 35.5	+17 09 50.7	(1)
Abell 68	0.255	00 37 06.8	+09 09 23.4	(2)
Abell 370	0.375	02 39 53.1	-01 34 54.8	(3)
MS 0451	0.55	04 54 10.6	-03 00 50.7	(4)
Abell 963	0.206	10 17 03.7	+39 02 49.2	(2)
Abell 1689	0.183	13 11 29.4	-01 20 28.7	(5)
Abell 2218	0.176	16 35 49.3	+66 12 43.5	(6)
Abell 2219	0.226	16 40 19.8	+46 42 41.9	(2)
Abell 2390	0.228	21 53 36.9	+17 41 43.4	(7)

REFERENCES. — (1) Kneib et al. (2003); (2) Smith et al. (2005) (3) Bézecourt et al. (1999); (4) Borys et al. (2004), (5) Limousin et al. *in prep*; (6) Kneib et al. (2004); (7) Swinbank et al. (2006)
[a] units of HH MM SS [b] units of +DD MM

The total counts associated with the dark current is given by

$$N_{DC} = n_{pix} dc(t_{int}/2) \qquad \text{(A-4)}$$

where n_{pix} is the number of pixels in the photometric aperture area and dc is the dark current in units of electrons per second per pixel. The number of pixels in the aperture is derived assuming a plate scale of $0''.15$. The typical dark current for near-IR imagers on 8-10 meter telescopes is 0.25 electrons s^{-1} pixel^{-1}; hence we adopt this value in our calculations.

The read noise contribution to the total noise is computed assuming Fowler sampling is used, which reduces the read noise by a factor of $\sqrt{4}/n_{read}$ where n_{read} is the number of reads at the beginning and end of each exposure. The total read noise in an aperture of size n_{pix} in the composite images is thus given by

$$RN = rn\sqrt{\frac{4\, n_{pix} n_{exp}}{n_{read}}} \qquad \text{(A-5)}$$

where rn is the detector read noise (for single readout) in units of electrons per pixel and n_{exp} is the number of exposures in the composite frame. We adopt a read noise of 10 electrons per pixel (Horton et al. 2004) for a single readout and assume the detector is read out 16 times per exposure.

The 5σ limiting flux is defined as the line flux for which the signal from the science source is a factor of five greater than the noise. For the instrument properties assumed, the 5σ limiting flux in a 10 hour narrowband survey is 3-9×10^{-18} erg cm^{-2} s^{-1} for a 10Å and 100Å narrowband filter, respectively. At z=9, this corresponds to a Lyman-α luminosity of 0.6-2×10^{42} erg s^{-1} assuming a magnification of $\times 5$. The survey volume is computed following equations 3 and 4 presented in §5.1.2 and assuming a magnification distribution for one of the most well-studied clusters, Abell 1689.

We also compute the efficiency of a conventional narrowband survey. The survey parameters are identical to those assumed for the lensing survey. The only difference is that in computing the limiting luminosity and survey volume, we do not fold in the magnification due to the lensing cluster.

The parameters chosen for the spectroscopic survey correspond to the properties of NIRSPEC on Keck. The limiting sensitivity in a spectroscopic survey is computed in the same way as for the narrowband survey. The spectroscopic survey strategy is described in §3.2. We divide the total integration time into many 1.5 hour observations; each 1.5 hour integration is further divided into nine 10 minute exposures. One key difference between the spectroscopic and narrowband survey is that the entire integration time is devoted to a single survey; hence, the ($t_{int}/2$) in the equations above become t_{int} for spectroscopic surveys.

Most of the parameters used in the spectroscopic S/N computation are identical to those used above. The read noise in each ten minute exposure is 25 electrons pixel^{-1} assuming 16 total reads; while slightly higher than in the narrowband survey described above, the noise is still sky-background dominated.

The median 5σ limiting flux for the spectroscopic survey is 8×10^{-18} erg cm^{-2} s^{-1}. We assume the longslit is placed along the critical lines of the lensing clusters listed in Table 1, which results in a significantly higher median magnification than in the narrowband survey. For a magnification of $\times 25$, this corresponds to a limiting Lyman-α luminosity of 4×10^{41} erg s^{-1}.

TABLE 2
NIRSPEC Survey Observations

Date	Cluster	Position Angle[a]	Integration time[b]
Aug 2004	Abell 2390 1	117	12.0
	Abell 2219 1	119.2	9.6
	Abell 68 1	330.	13.2
Jan 2005	MS 0451 1	120.9	11.4
	Abell 963 1	177.2	10.8
	Abell 963 2	175.0	5.4
	Abell 1689 1	43	5.4
June 2005	Abell 1689 1	43	3.6
	Abell 1689 2	205	10.8
	Abell 1689 3	139.1	10.8
	Abell 2218 1	153	10.8
	Abell 2218 2	134	5.4
	Abell 2219 1	119.2	5.4
	Abell 2219 2	160	16.2
	Abell 2390 2	109	10.2
	Abell 2390 3	20.0	6
Oct 2005	Abell 68 2	300	10.8
	Cl 0024 1	139.7	5.4
	Cl 0024 2	160.2	4.8
	MS 0451 2	100.1	7.2
	Abell 2390 3	20.0	5.4
	Abell 2390 4	90.0	4.8
	Abell 2219 2	160	2.4

[a] in degrees North through East [b] in ksec

TABLE 3
NIRSPEC Lyman α Candidates

Candidate	RA(J2000)	DEC(J2000)	flux (erg s^{-1} cm^{-2})	λ (μm)	$z_{\text{Ly}\alpha}$	$\text{Log}_{10}\,L_{\text{Ly}\alpha}$ (erg s^{-1})	Log_{10} Mag
A68c1	00 37 06.10	+09 09 18.7	$2.2\pm0.3\times10^{-17}$	1.254	9.32	$41.2^{+0.1}_{-0.7}$	$2.2^{+0.7}_{-0.1}$
A1689c1	13 11 31.85	−01 20 40.0	$2.3\pm0.3\times10^{-17}$	1.366	10.23	$42.3^{+0.02}_{-0.01}$	$1.2^{+0.01}_{-0.02}$
A1689c2	13 11 31.26	−01 20 29.8	$4.0\pm0.7\times10^{-17}$	1.173	8.65	$42.7^{+0.07}_{-0.08}$	$0.8^{+0.01}_{-0.03}$
A1689c3	13 11 28.43	−01 19 44.5	$4.1\pm0.6\times10^{-17}$	1.259	9.35	$42.1^{+0.06}_{-0.08}$	$1.5^{+0.04}_{-0.03}$
A2219c1	16 40 23.64	+46 42 26.5	$4.8\pm0.6\times10^{-17}$	1.215	8.99	$41.8^{+0.09}_{-0.07}$	$1.9^{+0.04}_{-0.07}$
A2219c2	16 40 23.04	+46 42 43.2	$2.1\pm0.3\times10^{-17}$	1.209	8.94	$42.0^{+0.06}_{-0.09}$	$1.3^{+0.06}_{-0.03}$

TABLE 4
Wavelengths of Additional Emission Lines for Low-z Scenarios

Line	z	$\lambda_{\text{Ly}\alpha}$ (μm)	$\lambda_{\text{[OII]}}$ (μm)	$\lambda_{\text{H}\beta}$ (μm)	$\lambda_{\text{[OIII]}}$ (μm)	$\lambda_{\text{H}\alpha}$ (μm)
Hα	0.85	0.2253	0.6905[a]	0.9007	0.9188/0.9277	1.2160
[OIII]	1.43[b]	0.2953	0.9051	1.1805	1.2043/1.2160	1.5939
	1.45[c]	0.2982	0.9139	1.1920	1.2160/1.2278	1.6093
Hβ	1.50	0.3042	0.9323	1.2160	1.2405/1.2525	1.6418
[OII]	2.26	0.3967	1.2160	1.5860	1.6180/1.6336	2.1413
Lyα	9.0	1.2160	3.7270	4.8610	4.9590/5.0070	6.5630

[a] Throughout the table, we take the luminosity-weighted value of [OII], λ=3727 Å, for conciseness. [b] λ=5007 Å [c] λ=4959 Å

TABLE 5
Constraints on Low-redshift Interpretations of Candidates

Line	z	$f_{Ly\alpha}$ $(10^{-17}$ erg cm^{-2} s$^{-1})$	$f_{[OII]}$ $(10^{-17}$ erg cm^{-2} s$^{-1})$	$f_{H\beta}$ $(10^{-17}$ erg cm^{-2} s$^{-1})$	$f_{[OIII]_1}/ f_{[OIII]_2}$ $(10^{-17}$ erg cm^{-2} s$^{-1})$	$f_{H\alpha}$ $(10^{-17}$ erg cm^{-2} s$^{-1})$
				Abell 68 c1		
Hα	0.91	N/A	0.63-2.4 (0.07)	0.79 (0.07)	N/A / N/A	N/A
[OIII]$_2$	1.51	N/A	N/A	0.31-2.8 (1)	0.73 (0.9)/ NA	0.4-13(2)
[OIII]$_1$	1.53	N/A	N/A	1.1-7.7 (6)	NA / 6.9 (5)	3.1-21 (2)
Hβ	1.58	N/A	N/A	NA	0.66-4.4 (5) / 1.8-15 (3)	6.2 (2)
[OII]	2.37	31 (0.02)	N/A	1.4 (5)	0.22-7.3 (7) / 2.2-5.1 (5)	N/A
				Abell 1689 c1		
Hα	1.06	N/A	N/A	N/A	N/A / N/A	N/A
[OIII]$_2$	1.71	N/A	N/A	0.33-2.9(6)	0.77(1) / N/A	N/A
[OIII]$_1$	1.72	N/A	N/A	1.2-7.7(0.9)	N/A / 6.9(4)	N/A
Hβ	1.79	N/A	N/A	N/A	0.69-4.6(20) / 1.8-16(100)	N/A
[OII]	2.64	N/A	N/A	N/A	N/A / N/A	N/A
				Abell 1689 c2		
Hα	0.78	N/A	N/A	N/A	N/A / N/A	N/A
[OIII]$_2$	1.33	N/A	N/A	N/A	1.3 (5) / N/A	N/A
[OIII]$_1$	1.36	N/A	N/A	N/A	N/A / 12(3)	N/A
Hβ	1.40	N/A	N/A	N/A	1.2-8.0(1) / 3.2-38(4)	N/A
[OII]	2.13	N/A	N/A	N/A	N/A / N/A	N/A
				Abell 1689 c3		
Hα	0.94	N/A	N/A	N/A	N/A / N/A	N/A
[OIII]$_2$	1.54	N/A	N/A	0.59-5.1 (8)	1.4 (2) / N/A	N/A
[OIII]$_1$	1.57	N/A	N/A	6.2-11 (2)	N/A / 12 (5)	N/A
Hβ	1.62	N/A	N/A	N/A	1.2-8.2 (3) / 3.3-29 (1)	N/A
[OII]	2.42	N/A	N/A	N/A	N/A / N/A	N/A
				Abell 2219 c1		
Hα	0.85	N/A	1.4-5.1 (0.3)	1.7 (1)	0.51-3.4 (0.4) / N/A	N/A
[OIII]$_2$	1.43	N/A	N/A	0.69-6.0(2)	1.6 (5) / N/A	1.9-17(2)
[OIII]$_1$	1.45	N/A	N/A	2.4-16(0.9)	N/A / 14(1)	6.7-45 (7)
Hβ	1.50	N/A	N/A	N/A	1.4-96 (2) / 3.8-34(0.9)	13 (3)
[OII]	2.26	35-130 (0.4)	N/A	1.6-6.0 (8)	1.8-3.2 (2) / 4.8-11 (5)	N/A
				Abell 2219 c2		
Hα	0.84	N/A	0.6-2.3 (0.4)	0.75 (1)	0.23-1.5(0.4) / 0.60-5.3 (0.5)	N/A
[OIII]$_2$	1.41	N/A	N/A	0.30-2.7 (2)	0.7 (3) / N/A	0.84-7.3 (10)
[OIII]$_1$	1.44	N/A	N/A	0.40−13 (1)	N/A / 6.3 (2)	0.4-13 (1)
Hβ	1.49	N/A	N/A	N/A	0.63-4.2(3) / 1.7-15(0.8)	5.9(4)
[OII]	2.24	N/A	15-58 (0.4)	0.70-2.6 (2)	0.79-2.4(4) / 2.1-4.9 (5)	N/A

Note. — The fluxes are predictions given the flux of the J-band feature and typical flux ratios for HII regions. The value in paranthesis is the limiting line flux at the corresponding wavelength (see §3.2 for details on how the limiting flux is computed). [OIII]$_1$ is $\lambda 4959$Å and [OIII]$_2$ is $\lambda 5007$Å
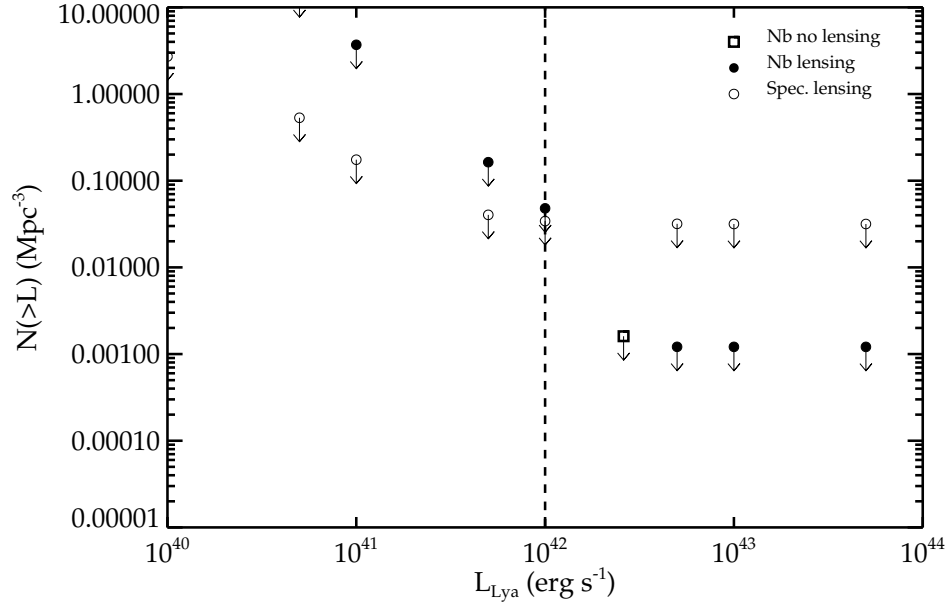
Fig. 1.— Comparison of different survey strategies for locating Lyman-α emitters with current instrumentation in seeing-limited conditions. Solid circles represent the minimum source abundance that a 60 hour spectroscopic lensing observing campaign (over 10 clusters) could constrain (at 5σ); while open circles correspond to the minimum source abundance that a narrowband imaging lensing survey could constrain in the same exposure time. Both survey techniques probe orders of magnitude fainter than a conventional narrowband survey (open square), albeit over much smaller volumes. At luminosities to the left of the dashed vertical line, the spectroscopic approach covers a larger volume, and thus it is significantly more efficient than narrowband imaging in constraining the abundance of the faintest ($\lesssim 1$ M$_\odot$ yr^{-1}) Lyman-α emitters.
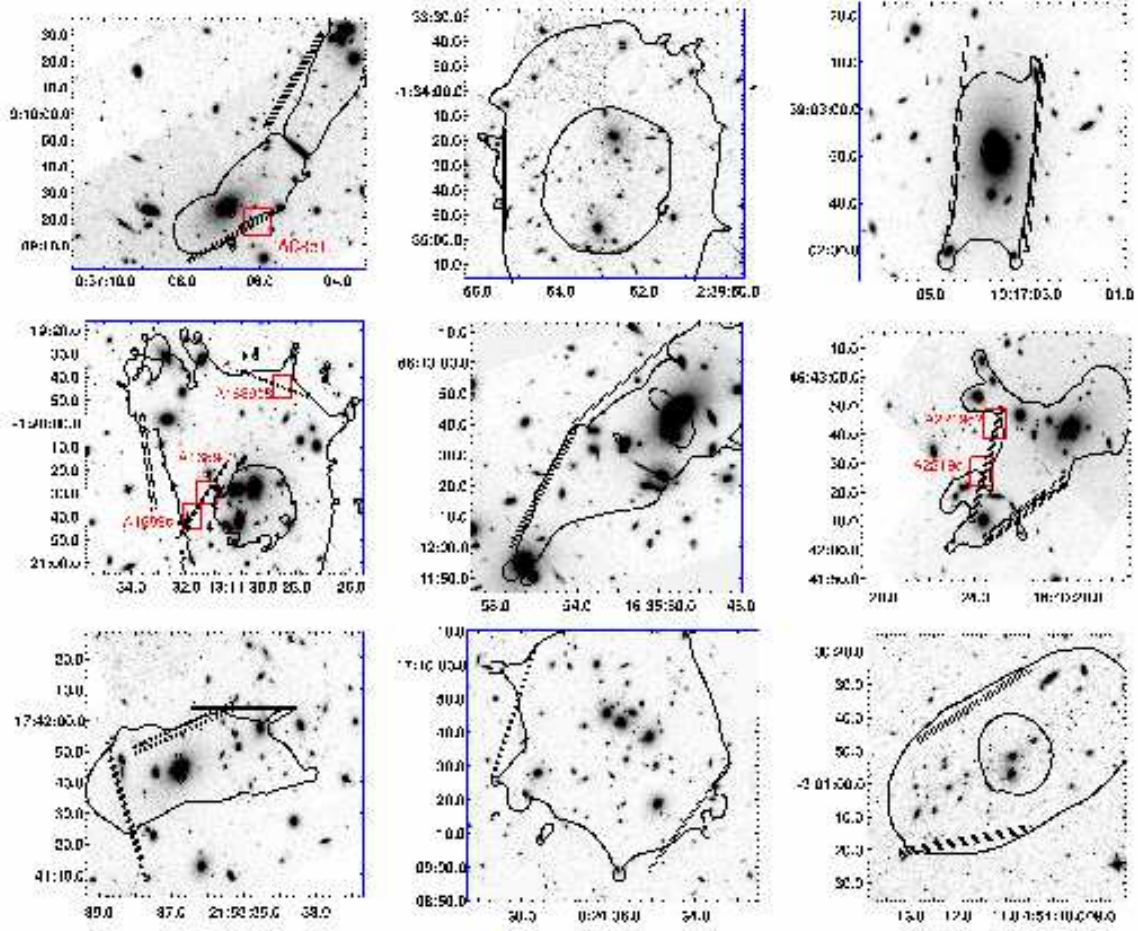
FIG. 2.— Survey clusters, with survey area and lensing critical curves. For each cluster, superposed on the *HST*/WFPC2 image are slit positions observed with NIRSPEC and the critical lines for a source at $z = 8$ (dotted lines). The solid curves bound areas where the magnification provided to $z = 8$ background sources exceeds a factor of 10. From left to right and top to bottom are Abell 68, Abell 370, Abell 963, Abell 1689, Abell 2218, Abell 2219, Abell 2390, CL 0024, MS 0451.

Stark et al.
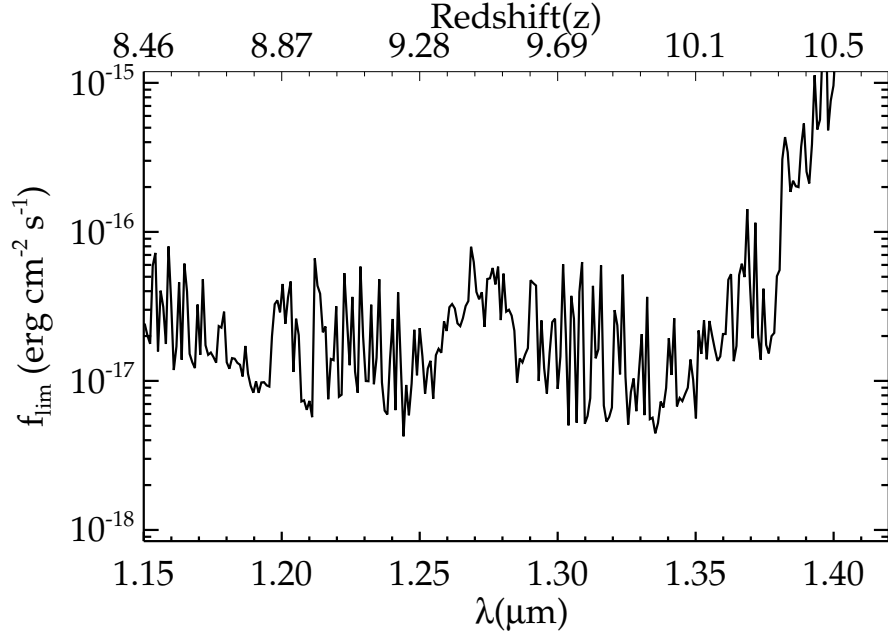
FIG. 3.— Limiting flux for detection of 5σ Lyman-α emission line for a typical NIRSPEC J band exposure. The top axis denotes the redshift corresponding to observed Lyman-α at the wavelength along the bottom axis. **OH bands lie throughout the J-band spectrum, signficantly increasing the limiting flux at those wavelengths. The widest band occurs in the middle of the spectrum at $\simeq 1.26 - 1.28\mu m$.**
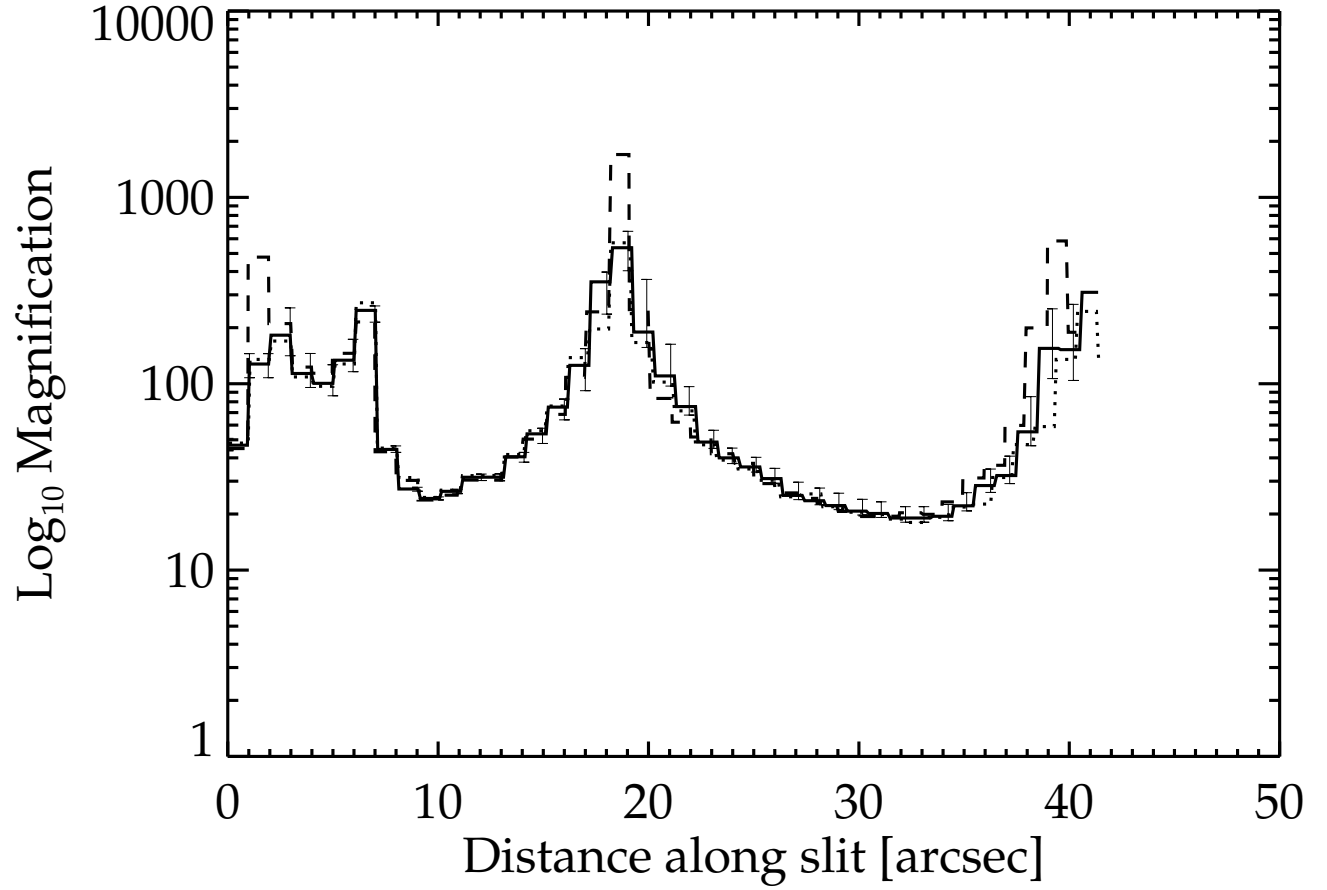
FIG. 4.— Lensing magnification provided to background sources as a function of NIRSPEC slit position and redshift. This figure shows the amplification at one of the slit positions along the critical line of Abell 2219. The solid line corresponds to the amplification provided to background sources at z=9 whereas the dotted and dashed line denotes that provided to sources at z=8.5 and 10.0, respectively. The error in lensing magnification is plotted as a function of NIRSPEC slit position for sources at z=9. The error does not vary significantly as a function of source redshift. Even allowing for uncertainty in the mass model, the magnification is still very high across the entire slit.
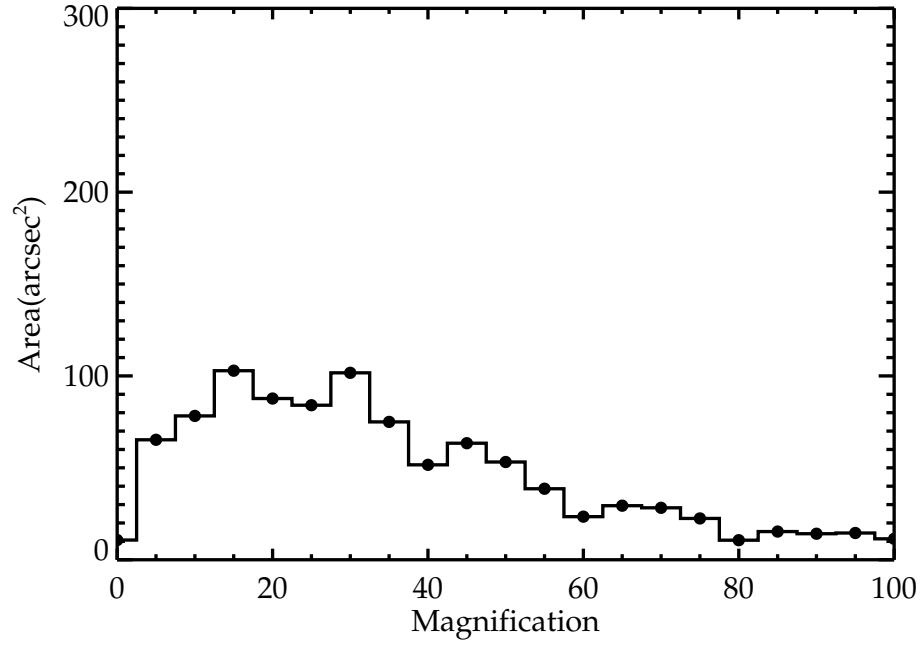
FIG. 5.— Distribution of lensing magnfication across our total survey area. The median magnification across our survey area is $\simeq 20$, about a factor of 2 larger than in a similar optical spectroscopic lensing survey (Santos et al. 2004) **(see §3.4 for explanation)**. A non-negligible fraction of each slit is magnified by larger than this factor.
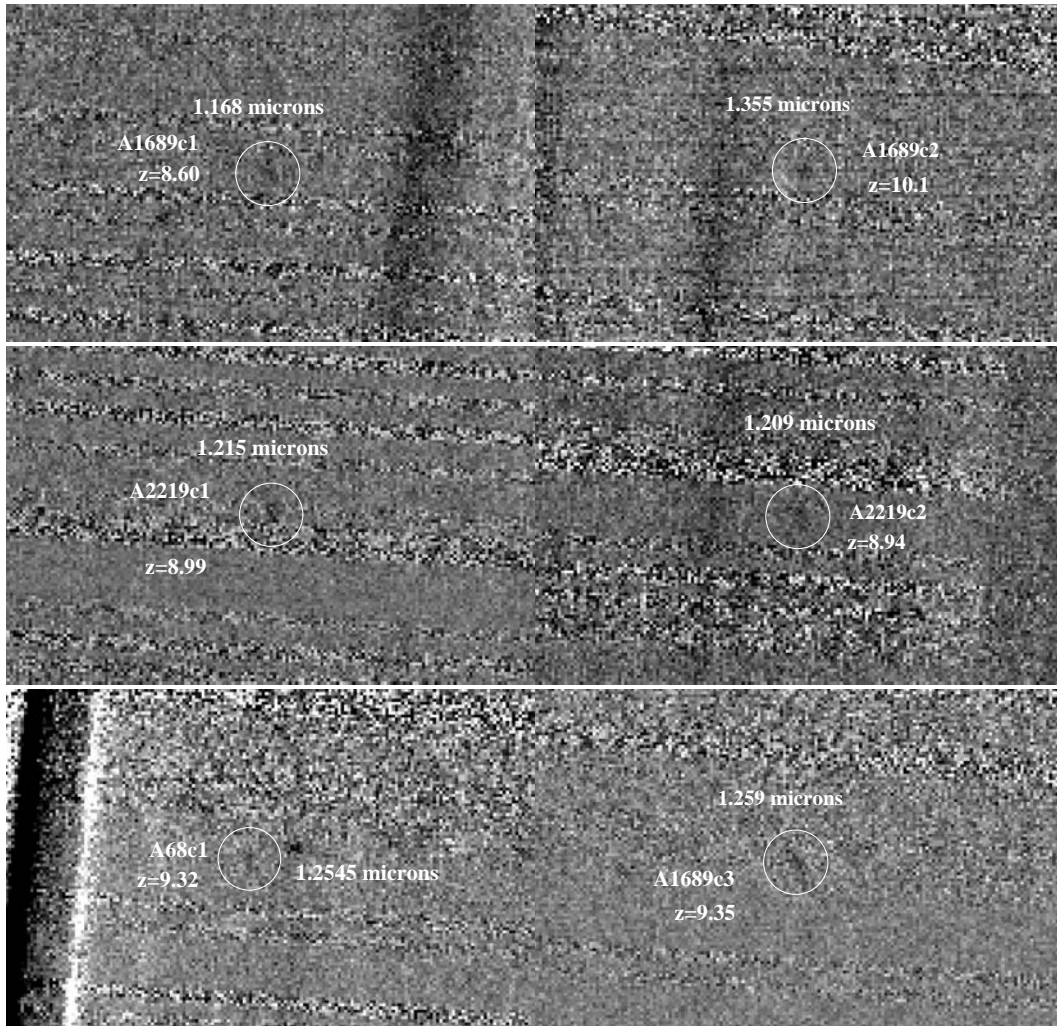
Fig. 6.— Candidate Lyman-α emitters, each undetected in deep optical HST data. If Lyman-α, the emission line redshifts range between $z = 8.7$ and $z = 10.2$. Line fluxes range between $2 - 5 \times 10^{-17}$ erg cm^{-2} s^{-1} implying intrinsic (unlensed) star formation rates of 0.2-5 M$_\odot$ yr^{-1}, for nominal source assumptions.
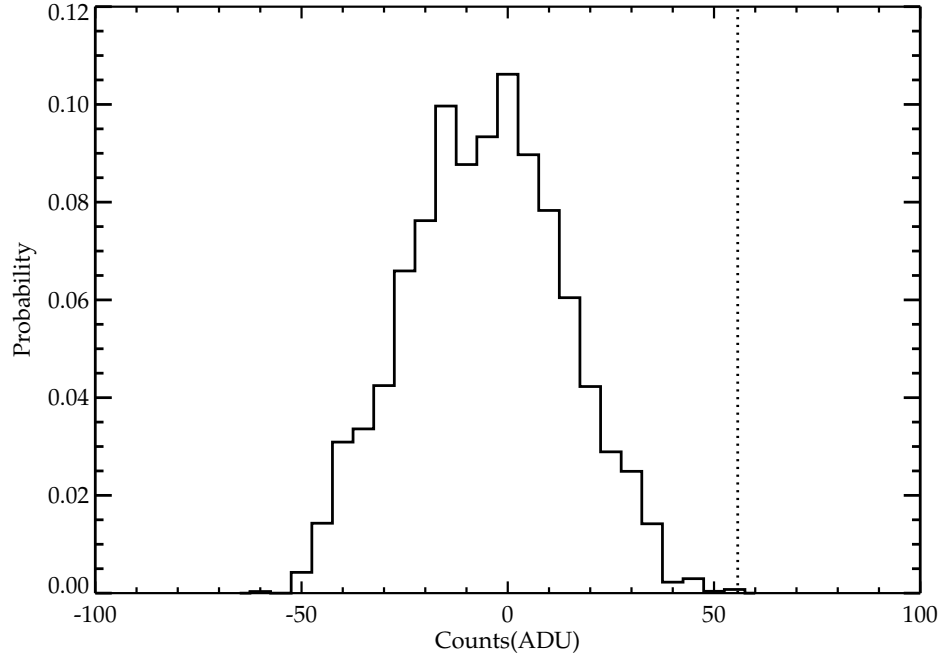
FIG. 7.— Normalized histogram of summed flux in randomly placed apertures in clean regions of sky-subtracted spectra. The dotted line represents value of a typical candidate Lyman-α emitter. The frequency of features with fluxes on par with the candidates is 0.02%, consistent with a $\simeq 4\sigma$ detection assuming a Gaussian distribution of noise.
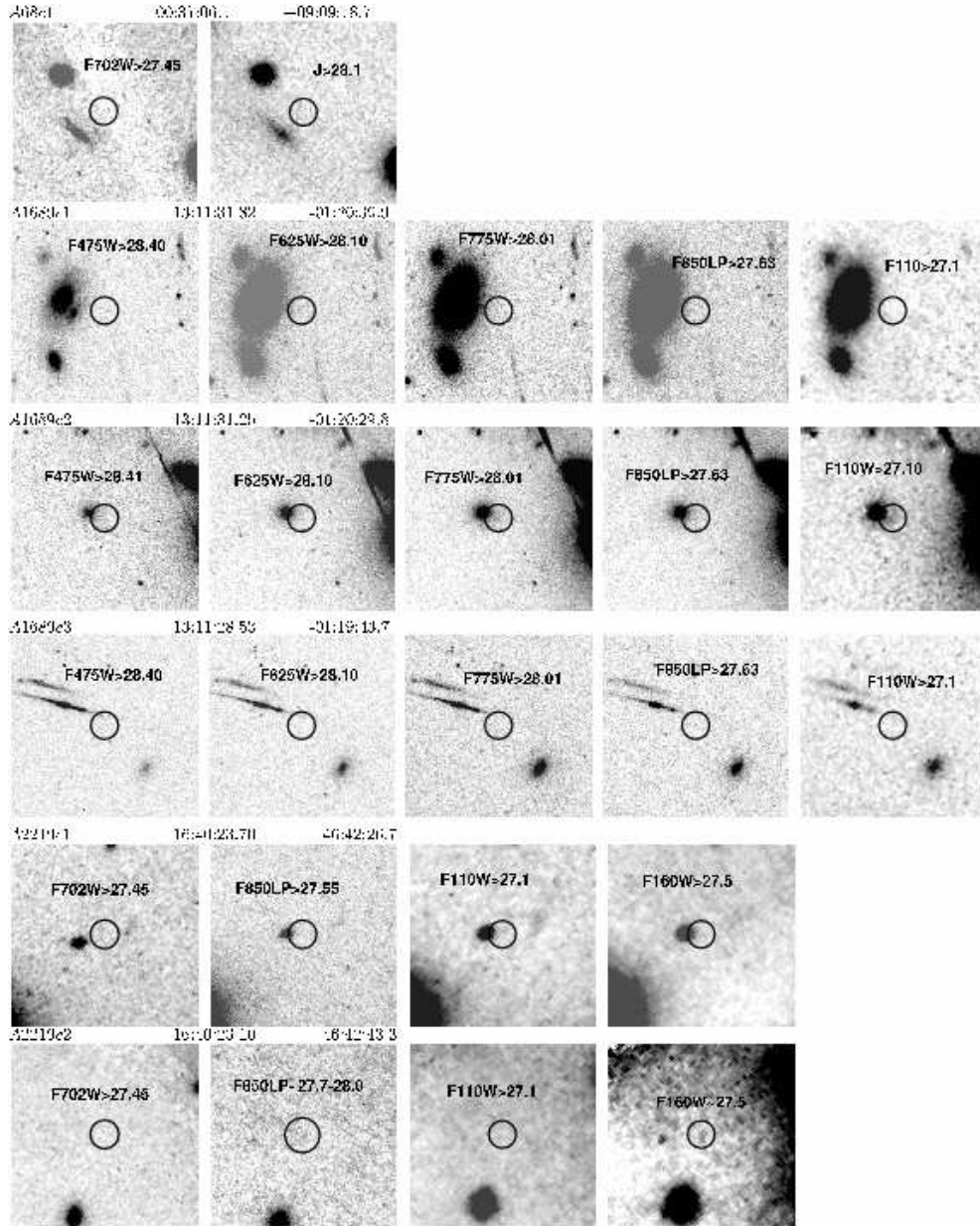
FIG. 8.— Deep broadband images of the locations of the candidate J-band emission features. None of the candidates have *definitive* detections in the optical; although A2219c2 is very marginally detected in the z'_{F850LP} and H_{F160W} bands. Three of the candidates are located within several arcseconds of brighter objects (A2219c1, A1689c1, and A1689c2); however in both cases, our registration is known to sufficient precision to rule out the possibility that the J-band emission features emanate from the bright objects. The lack of detection in very deep near-IR images suggests that if these candidates are at $z \simeq 9$, then their rest-frame UV continuum emission is very faint.
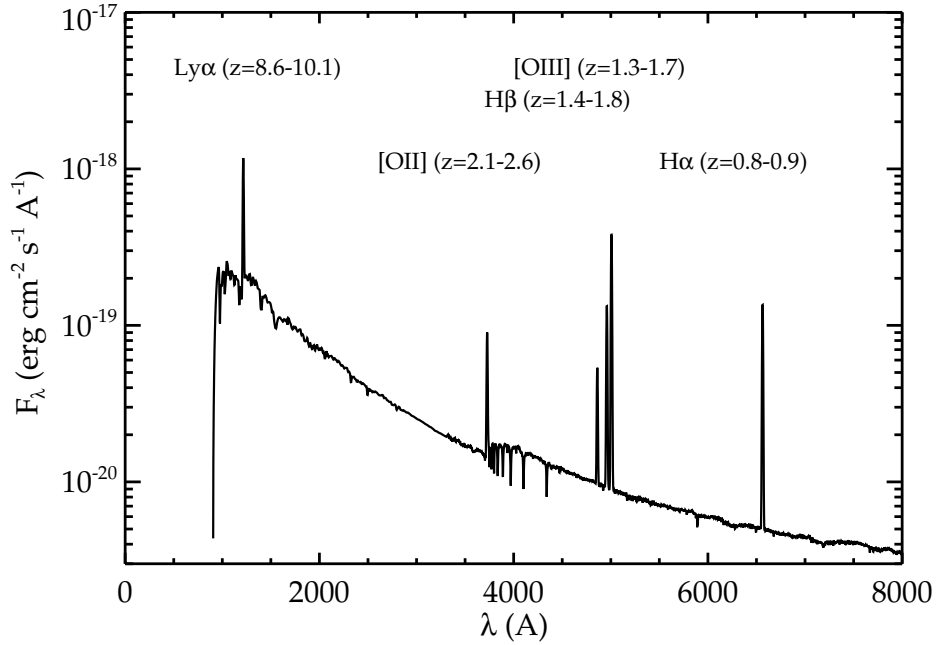
Fig. 9.— Most likely emission features and corresponding redshifts of the J-band emission features. If the line lies in the rest-frame optical ([OII], Hβ, [OIII], Hα), then additional emission features should be present in optical or near-infrared spectroscopy. If, on the other hand, the line is Lyman-α at z=8.5-10, then additional powerful emission lines will have been redshifted into the mid-infrared, making confirmation very difficult.
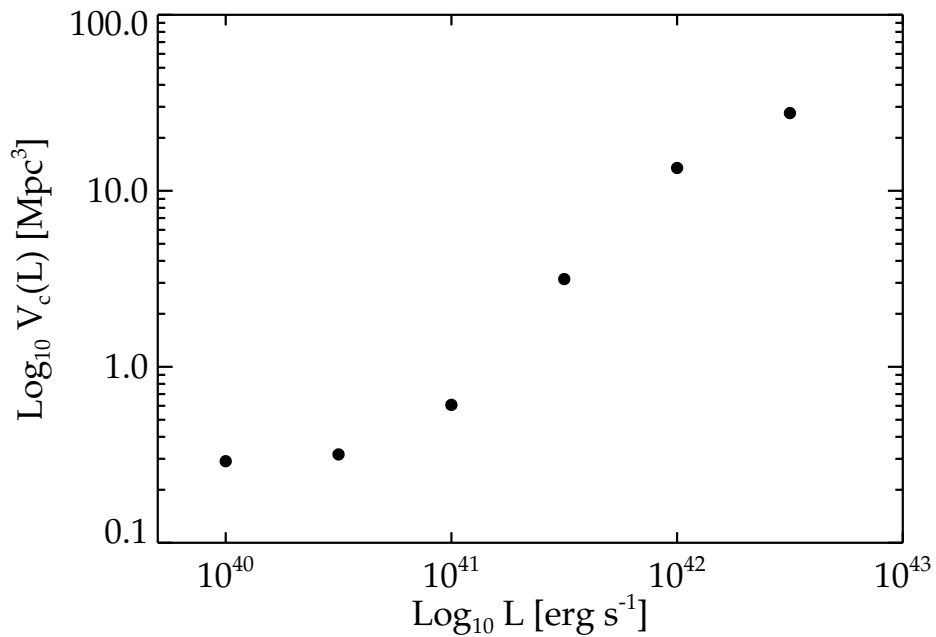

Fig. 10.— Survey volume (comoving) sensitive to sources with Lyman-α luminosity L. The volumes observed are very small as a result of the small area of the spectroscopic slit and the decrease in survey area resulting from gravitational lensing.
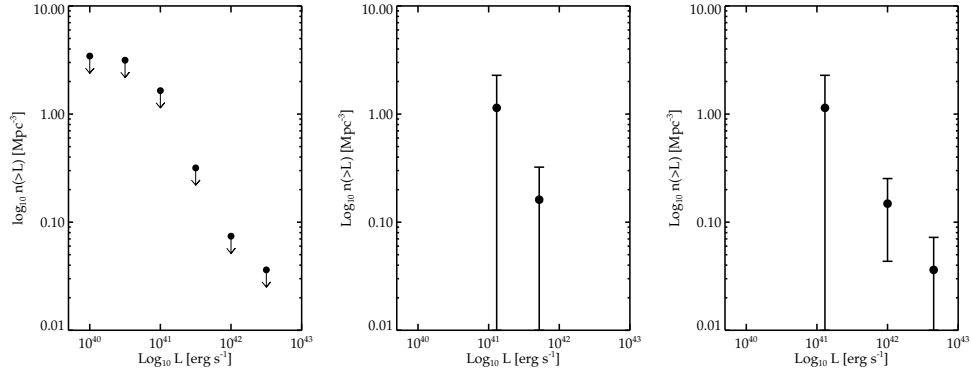
FIG. 11.— Constraints on number density of $8.5<z<10.2$ sources with Lyman-α luminosity brighter than L. Left: The 5σ upper limit to the abundance of low luminosity Lyman-α emitters is presented assuming none of our candidate Lyman-α emitters is real. Middle: The cumulative abundance of Lyman-α emitters if two of the candidates (A68c1 and A2219c1) are real. Right: The cumulative abundance of Lyman-α emitters assuming each of the six candidates is a Lyman-α emitter. If even one candidate is real, the inferred abundance of low luminosity Lyman-α emitters at $z \simeq 9$ would be very high.
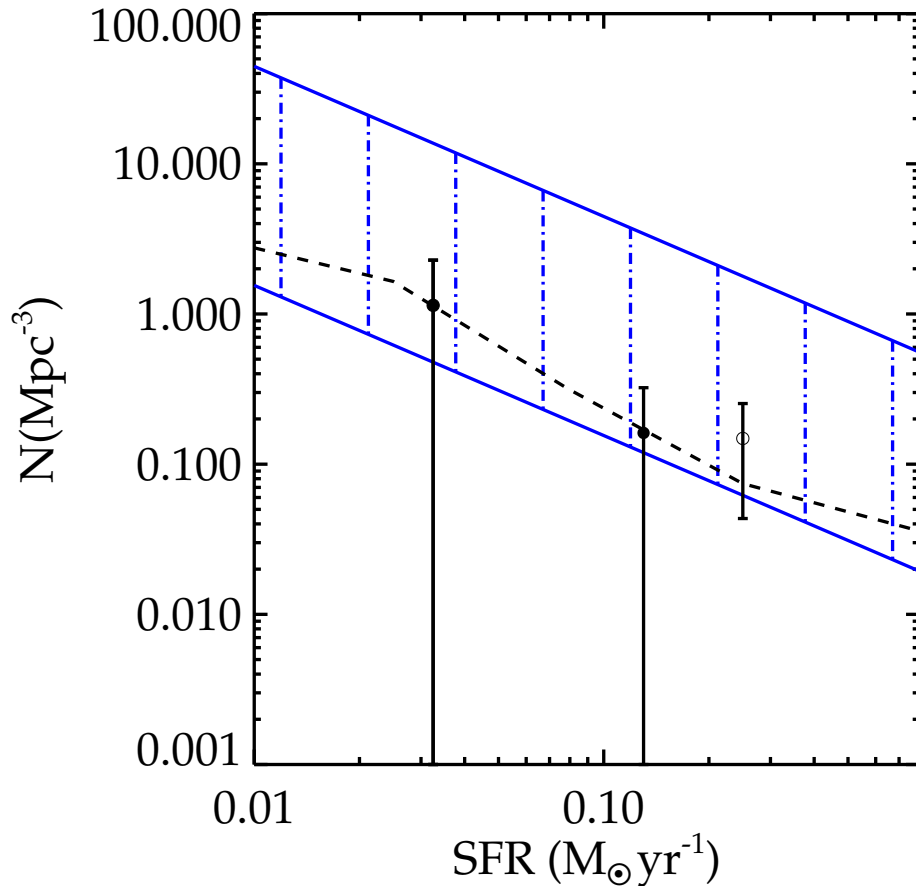

FIG. 12.— Abundance of sources required for reionization assuming a single population of star-forming galaxies dominates the process (blue swath) compared the observed abundances (a) if all the candidates are real (open circles), (b) two of the candidates are real (solid circles), or (c) if none of the candidates are real (dotted line). The abundance constraints for case a and case b are identical for the two lowest luminosity bins plotted in the figure. The range for the abundance of sources required for reionization is determined assuming $f_c=0.5$, $\Delta t_{reion}=575$ Myr, and B=10 for the lower locus of points and $f_c=0.02$, $\Delta t_{reion}=250$ Myr, and B=5 for the upper locus of points. If two or more of the candidates are real, then it appears that intrinsically faint galaxies may play a dominant role in the reionization of neutral hydrogen.